NASA Technical Paper 1619

Application of a Numerically Generated Orthogonal Coordinate System to the Solution of Inviscid Axisymmetric Supersonic Flow Over Blunt Bodies

H. Harris Hamilton II and Randolph A. Graves, Jr.

MARCH 1980

NASA

NASA Technical Paper 1619

Application of a Numerically Generated Orthogonal Coordinate System to the Solution of Inviscid Axisymmetric Supersonic Flow Over Blunt Bodies

H. Harris Hamilton II and Randolph A. Graves, Jr.
Langley Research Center
Hampton, Virginia

National Aeronautics
and Space Administration

**Scientific and Technical
Information Office**

1980

SUMMARY

A numerically generated orthogonal coordinate system (with the body surface and shock wave as opposite boundaries) has been applied with a time asymptotic method to obtain steady-flow solutions for axisymmetric inviscid flow over several blunt bodies including spheres, paraboloids, ellipsoids, hyperboloids, hemisphere cylinders, spherically blunted cones, and a body with a concavity in the stagnation region. Comparisons with experimental data and the results of other computational methods have demonstrated that accurate solutions can be obtained with this approach. The numerically generated orthogonal coordinate system used in the present paper should prove useful for applications to complex body shapes, particularly those with concave regions. In addition, the use of the present orthogonal coordinate system simplifies the form of the governing equations and simplifies the application of boundary conditions at the body surface and shock wave.

INTRODUCTION

Previous investigations of the direct blunt-body problem have demonstrated the utility of treating the bow shock wave as a discrete discontinuity. (See, for example, refs. 1 to 5.) In each of these studies, some form of coordinate transformation was used to map the physical space within the shock layer into a rectangular computational domain, with the bow shock wave as one boundary and the body surface as the opposite boundary. These transformations generally produce a nonorthogonal coordinate system in the physical space which complicates the form of the equations of motion. However, they usually produce a uniform grid system for calculating the flow-field solution and simplify the application of the boundary conditions at the shock wave and the body surface.

Recently, Graves (ref. 6) applied a method for numerically generating an orthogonal coordinate system between two arbitrary continuous curves. By allowing one of the curves to be the body surface and the other to be the bow shock wave (which can move with time), this method can be used to construct an orthogonal coordinate for solving the blunt-body problem. An orthogonal coordinate system of this type leads to a much simpler form of the equations of motion and further simplifies the application of boundary conditions at the body surface and the shock wave. In addition, this type of coordinate system can be applied to complex body shapes, including bodies with concave regions.

The purpose of the present paper is to explore the application of the numerically generated orthogonal coordinate system presented in reference 6 to flow-field problems. For this purpose, the inviscid, axisymmetric supersonic flow over a blunt-nose body will be investigated.

SYMBOLS

a	speed of sound, $\hat{a}/\hat{V}_\infty^2$; also length of z-axis for ellipse
B_b	bluntness parameter
b	length of r-axis for ellipse
c_p	specific heat at constant pressure
c_v	specific heat at constant volume
d	diameter of cylinder, $\hat{d}/\hat{L}$
h_1, h_2	metric coefficients in ξ- and η-directions, $\hat{h}_1/\hat{L}$ and $\hat{h}_2/\hat{L}$, respectively
h_3	metric coefficient in circumferential direction, $\hat{h}_3/\hat{L}$
I	static enthalpy, $\hat{I}/\hat{V}_\infty^2$
i	index for ξ-direction, $\xi = (i - 1)\ \Delta\xi$
j	index in η-direction, $\eta = (j - 1)\ \Delta\eta$
$\hat{L}$	dimensional characteristic length, m
M	Mach number
p	pressure, $\hat{p}/\hat{\rho}_\infty\hat{V}_\infty^2$
R_b	body nose radius, $\hat{R}_b/\hat{L}$
R	radius defined in figure 1, $\hat{R}/\hat{L}$
s	coordinate arc length, $\hat{s}/\hat{L}$
t	time, $\hat{t}\hat{V}_\infty/\hat{L}$
u	velocity component in ξ-direction, $\hat{u}/\hat{V}_\infty$
V_s	shock velocity, $\hat{V}_s/\hat{V}_\infty$
V_∞	free-stream velocity, $\hat{V}_\infty/\hat{V}_\infty = 1$
$\hat{V}_\infty$	dimensional free-stream velocity, m/sec
V_n	component of velocity normal to shock wave, $\hat{V}_n/\hat{V}_\infty$
V_t	component of velocity tangent to shock wave, $\hat{V}_t/\hat{V}_\infty$

v	velocity component in η-direction, $\hat{v}/\hat{v}_\infty$
z,r	Cartesian coordinate system (see fig. 1), $\hat{z}/\hat{L}$, $\hat{r}/\hat{L}$
z_p	location of pole for ϕ coordinate (see fig. 1), $\hat{z}_p/\hat{L}$
β	shock wave angle
γ	ratio of specific heats c_p/c_v
ΔR	shock-layer thickness in polar coordinates, $\Delta\hat{R}/\hat{L}$
Δt	time increment
$\Delta\eta$	increment in η-coordinate
$\Delta\xi$	increment in ξ-coordinate
ξ,η	orthogonal coordinate system (see fig. 2)
ρ	density, $\hat{\rho}/\hat{\rho}_\infty$
ϕ	angular coordinate defined in figure 1

Superscripts:

$(\hat{})$	dimensional quantity
$(\bar{})$	predicted quantity

Subscripts:

max	maximum
o	stagnation
s	shock
∞	free stream

METHOD OF SOLUTION

The problem is to compute the inviscid, axisymmetric supersonic flow over a blunt-nose body. Solutions are to be obtained throughout the subsonic region and downstream into the supersonic region (fig. 1).

Coordinate System

Using the method described in reference 6, a general orthogonal coordinate system was numerically constructed between the body surface ($\eta = 0$) and the bow shock wave ($\eta = 1$) extending from the stagnation streamline ($\xi = 0$) to a downstream outflow boundary ($\xi = 1$) located within the supersonic portion of the shock layer (fig. 2). The line element for this orthogonal coordinate system (ξ,η) is given by the equation

$$ds^2 = h_1{}^2 d\xi^2 + h_2{}^2 d\eta^2 \tag{1}$$

where h_1 is the metric coefficient in the ξ-direction and h_2 is the metric coefficient in the η-direction.

The ξ-coordinates can be chosen so that grid points are equally spaced along the body surface in the physical plane or so that they may be concentrated in regions of large gradients. Similarly, the η-coordinates can be chosen so that grid points are equally spaced between the body and the shock wave or so that they may be concentrated in any desired region. However, in both cases the grid system is uniform in both the ξ- and η-directions in the computational plane (fig. 3). Any nonuniformity in the physical plane is taken care of by the metric coefficients h_1 and h_2, which are calculated each time the coordinate system is calculated.

Flow-Field Equations

The partial differential equations governing the axisymmetric compressible flow of an inviscid nonconducting fluid in general orthogonal coordinates are

Continuity:

$$\frac{\partial \rho}{\partial t} + \frac{u}{h_1}\frac{\partial \rho}{\partial \xi} + \frac{v}{h_2}\frac{\partial \rho}{\partial \eta} + \rho\left[\frac{1}{h_1}\frac{\partial u}{\partial \xi} + \frac{1}{h_2}\frac{\partial v}{\partial \eta} + \frac{u}{h_1 h_2}\frac{\partial h_2}{\partial \xi} + \frac{v}{h_1 h_2}\frac{\partial h_1}{\partial \eta} + \left(\frac{u}{h_1 h_3}\frac{\partial h_3}{\partial \xi} + \frac{v}{h_2 h_3}\frac{\partial h_3}{\partial \eta}\right)\right] = 0 \tag{2}$$

ξ-momentum:

$$\frac{\partial u}{\partial t} + \frac{u}{h_1}\frac{\partial u}{\partial \xi} + \frac{v}{h_2}\frac{\partial u}{\partial \eta} - v\left(\frac{v}{h_1 h_2}\frac{\partial h_2}{\partial \xi} - \frac{u}{h_1 h_2}\frac{\partial h_1}{\partial \eta}\right) + \frac{1}{\rho}\left(\frac{1}{h_2}\frac{\partial p}{\partial \xi}\right) = 0 \tag{3}$$

η-momentum:

$$\frac{\partial v}{\partial t} + \frac{u}{h_1}\frac{\partial v}{\partial \xi} + \frac{v}{h_2}\frac{\partial v}{\partial \eta} + u\left(\frac{v}{h_1 h_2}\frac{\partial h_2}{\partial \xi} - \frac{u}{h_1 h_2}\frac{\partial h_1}{\partial \eta}\right) + \frac{1}{\rho}\left(\frac{1}{h_2}\frac{\partial p}{\partial \eta}\right) = 0 \tag{4}$$

The preceding system of equations in general orthogonal coordinates is much simpler than the system of equations that is obtained if the space between the body and the shock wave is mapped into a rectangular computational domain (refs. 1 to 3), where the resulting coordinate system in physical space is nonorthogonal.

In order to close this system of equations, the integrated form of the steady-flow energy equation

$$I_\infty + \frac{u^2 + v^2}{2} = I_o \tag{5}$$

is used along with the ideal gas equation of state

$$p = \rho\left(\frac{\gamma - 1}{\gamma}\right)I \tag{6}$$

Steady-flow solutions are obtained by integrating the system of equations (2) to (6) in time, from an assumed set of initial conditions, until steady state is reached. Since the integrated form of the energy equation (eq. (5)) is being used, the results are not accurate during the transient phase of the solution. However, equation (5) becomes more accurate as the

steady state is approached and the correct converged steady-flow solution is obtained. Using the energy equation in this form speeds up the computational procedure.

Along the stagnation streamlines $u = h_3 = 0$ and $\partial h_3/\partial \xi = h_1$; thus the terms $\dfrac{u}{h_1 h_3}\dfrac{\partial h_3}{\partial \xi}$ and $\dfrac{v}{h_2 h_3}\dfrac{\partial h_3}{\partial \eta}$ appearing in equation (2) are of the indefinite form (0/0). Taking the limit of these terms as $\xi \to 0$ by using L'Hôpital's rule

$$\lim_{\xi \to 0}\left(\frac{u}{h_1 h_3}\frac{\partial h_3}{\partial \xi}\right) = \lim_{\xi \to 0}\left(\frac{\partial u/\partial \xi}{\partial h_3/\partial \xi}\right) = \frac{1}{h_1}\frac{\partial u}{\partial \xi} \tag{7}$$

$$\begin{aligned}\lim_{\xi \to 0}\left(\frac{v}{h_2 h_3}\frac{\partial h_3}{\partial \eta}\right) &= \frac{v}{h_2}\left\{\lim_{\xi \to 0}\left[\frac{\dfrac{\partial}{\partial \xi}\left(\dfrac{\partial h_3}{\partial \eta}\right)}{\partial h_3/\partial \xi}\right]\right\} \\ &= \frac{v}{h_2}\left\{\lim_{\xi \to 0}\left[\frac{\dfrac{\partial}{\partial \eta}\left(\dfrac{\partial h_3}{\partial \xi}\right)}{\partial h_3/\partial \xi}\right]\right\} \\ &= \frac{v}{h_1 h_2}\frac{\partial h_1}{\partial \eta}\end{aligned} \tag{8}$$

Thus on the stagnation line ($\xi = 0$), the limiting form of the continuity equation (2) becomes

$$\frac{\partial \rho}{\partial t} + \frac{v}{h_2}\frac{\partial \rho}{\partial \eta} + \rho\left[\frac{1}{h_2}\frac{\partial v}{\partial \eta} + 2\left(\frac{1}{h_1}\frac{\partial u}{\partial \xi} + \frac{v}{h_1 h_2}\frac{\partial h_1}{\partial \eta}\right)\right] \qquad (\xi = 0) \tag{9}$$

Equations (2) to (9) are written in nondimensional form using the following definition for the nondimensional variables:

$$\left.\begin{aligned} u &= \hat{u}/\hat{V}_\infty & t &= \hat{t}\hat{V}_\infty/\hat{L} \\ v &= \hat{v}/\hat{V}_\infty & h_1 &= \hat{h}_1/\hat{L} \\ \rho &= \hat{\rho}/\hat{\rho}_\infty & h_2 &= \hat{h}_2/\hat{L} \\ I &= \hat{I}/\hat{V}_\infty^2 & h_3 &= \hat{h}_3/\hat{L} \\ p &= \hat{p}/\hat{\rho}_\infty\hat{V}_\infty^2 \end{aligned}\right\} \qquad (10)$$

Finite-Difference Scheme

The solution of the flow field is obtained by integrating the compressible, time-dependent Euler equations described in the previous section. The integration is carried out using the explicit finite-difference scheme of Brailovskaya (ref. 7).

Using the following computational module

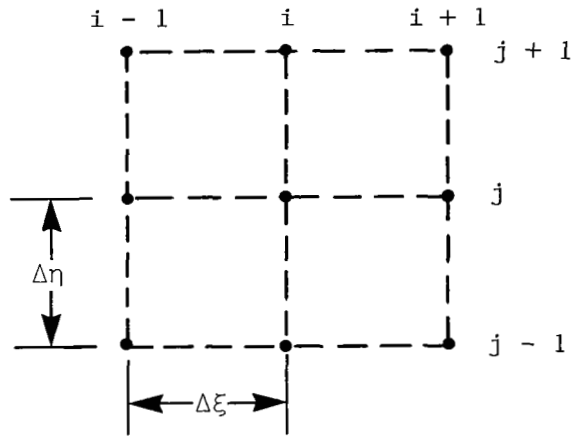

this two-step difference scheme can be represented as follows:

Predictor step:

$$\overline{F^{t+\Delta t}_{i,j}} = F^{t}_{i,j} + \Delta t\left(\frac{\partial F}{\partial t}\right)^{t}_{i,j} \tag{11a}$$

Corrector step:

$$F^{t+\Delta t}_{i,j} = F^{t}_{i,j} + \Delta t\left(\frac{\partial F}{\partial t}\right)^{\overline{t+\Delta t}}_{i,j} \tag{11b}$$

where F can represent ρ, u, or v. The time derivatives appearing in equations (11a) and (11b) are obtained from equations (2) to (4). The spatial derivatives in equations (2) to (4) are evaluated using central difference formulas except at the boundaries where three-point, one-sided difference formulas are used.

The numerical stability limit for this difference scheme is the well-known CFL condition given by the equation (ref. 8)

$$(\Delta t)_{max} = \frac{1}{\frac{|u|}{h_1\ \Delta\xi} + \frac{|v|}{h_2\ \Delta\eta} + a\sqrt{\frac{1}{(h_1\ \Delta\xi)^2} + \frac{1}{(h_1\ \Delta\eta)^2}}} \tag{12}$$

The local maximum time step at each grid point is calculated by using equation (12), and then a fraction of the local value (usually 50 to 80 percent) is applied at each grid point to advance the solution in time. This leads to an inaccurate representation of the time-dependent nature of the solution, but it has been found to accelerate convergence by a factor of approximately 1.5 to 2 when compared with using the minimum global time step.

Boundary and Initial Conditions

The boundary condition of no flow normal to the body surface is

$$v = 0 \qquad (\eta = 0) \tag{13}$$

since the body surface is the inner boundary of an orthogonal coordinate system. The remaining properties at the surface are computed using three-point forward

differences to calculate the spatial derivatives in both the predictor and corrector steps of the finite-difference scheme described in the previous section.

At the outflow boundary ($\xi = 1$) and the shock wave ($\eta = 1$), three-point backward differences (away from the boundary) are used. At the shock wave, the pressure thus calculated is used with the shock-wave relations (described in the next section) to calculate the shock velocity and then to update all other properties at the shock wave.

Along the stagnation streamline ($\xi = 0$), the following conditions are set:

$$\left.\begin{aligned} u &= 0 \\ \frac{\partial v}{\partial \xi} = \frac{\partial p}{\partial \xi} &= \frac{\partial \rho}{\partial \xi} = \frac{\partial h_2}{\partial \xi} = 0 \end{aligned}\right\} \tag{14}$$

and the remaining derivatives are computed by taking into account the asymmetry in the u-component of velocity.

To start the solution, a shock-wave shape is assumed and the shock-wave velocities are set equal to zero. Properties at the shock wave are computed from the shock-wave relations. Properties on the body surface are computed from modified Newtonian theory, assuming that the entropy is constant on the surface. Properties at a constant value of ξ across the shock layer are approximated by linearly interpolating between the values at the shock wave and the body surface.

Solution for Shock Wave

A method similar to that used by Weilmuenster and Hamilton (ref. 9) has been used to track the movement of the shock wave during the transient portion of the solution. The method can be summarized as follows (details are given in the appendix). First the pressure is computed on the downstream side of the shock wave by using the two-step difference scheme described previously. With the pressure at the shock wave p_s known, the density is computed from the equation

$$\frac{1}{\rho_s} = \frac{I_\infty + \frac{1}{2}(p_s - p_\infty)}{p_s\left(\frac{\gamma}{\gamma - 1}\right) - \frac{1}{2}(p_s - p_\infty)} \tag{15}$$

and then the shock velocity is computed with the equation

$$V_s = (V_n)_\infty - \sqrt{\frac{p_s - p_\infty}{1 - \frac{1}{\rho_s}}} \tag{16}$$

where V_s and $(V_n)_\infty$ are defined in the sketches in the appendix. Next, the movement of the shock wave is computed from the following differential equations:

$$\frac{dz_s}{dt} = V_s \sin \beta_s \tag{17a}$$

$$\frac{dr_s}{dt} = -V_s \cos \beta_s \tag{17b}$$

where

$$\beta_s = \tan^{-1} (dr_s/dz)$$

by using the following two-step finite-difference approximations:

Predictor step:

$$(z_s)^{\overline{t+\Delta t}} = z_s^t + \Delta t(V_s \sin \beta_s)^t \tag{18a}$$

$$(r_s)^{\overline{t+\Delta t}} = r_s^t - \Delta t(V_s \cos \beta_s)^t \tag{18b}$$

Corrector step:

$$(z_s)^{t+\Delta t} = z_s^t + \frac{\Delta t}{2}\left[(V_s \sin \beta_s)^t + \overline{(V_s \sin \beta_s)^{t+\Delta t}}\right] \tag{19a}$$

$$(r_s)^{t+\Delta t} = r_s^t - \frac{\Delta t}{2}\left[(V_s \cos \beta_s)^t + \overline{(V_s \cos \beta_s)^{t+\Delta t}}\right] \tag{19b}$$

The coordinate system generator is used to update the shock wave after the predictor step and the entire coordinate system after the corrector step. As the solution approaches convergence, the shock velocity approaches zero and the shock wave remains essentially fixed in space. The shock velocities at convergence are generally less than 10^{-3} in magnitude.

Convergence and Computational Time

The average change in density from one time step to the next was used to determine convergence. Based on the results of several test cases, it was found that the solution was converged when the average change in density was less than 2×10^{-5}. For the cases presented in the present paper, this generally required from 400 to 600 time steps.

From timing studies on the Control Data CYBER 175 computer system, it has been found that approximately 3.4×10^{-4} sec/point/step were required to compute the flow field and approximately 7.8×10^{-4} sec/point/step were required to compute the coordinate system. Thus, in the present nonoptimized computer code, approximately 70 percent of the time is spent computing the coordinate system. One obvious method of improving the overall efficiency is to update the coordinate system less frequently. For example, it is possible to update the shock wave after each time step and hold the remainder of the coordinate system fixed for several time steps before recomputing. This would greatly reduce the percentage of computational time spent on generating the coordinate system.

Body Geometry

Most of the body geometrics that are considered in the present paper have a projection in the $\hat{z},\hat{r}$ plane that is described by the equation for a general conic section

$$\hat{r}^2 = 2\hat{R}_b\hat{z} - B_b\hat{z}^2 \tag{20}$$

where $\hat{R}_b$ is the radius of curvature at $\hat{z} = 0$ and B_b is a bluntness parameter. The bluntness parameter B_b characterizes the eccentricity of the conic section. Its significance is better understood if it is noted that $B_b < 0$ generates a hyperbola, $B_b = 0$ generates a parabola, and $B_b > 0$ generates an ellipse (with $B_b = 1$ for the special case of a circle). For an ellipse, B_b is related to the ratio of major to minor axis (b/a) by the relation

$$B_b = (b/a)^2 \tag{21}$$

Some of the body shapes considered in the present paper were spherically blunted cones. These body shapes were generated using equation (20) for the nose, with $B_b = 1$, followed by a straight-line segment tangent to the nose at the appropriate cone angle.

One body shape considered had a reverse curvature at the nose matched to a 30° conical afterbody at the point $\hat{z} = 0$ and $\hat{r} = 1$ and defined by the equation

$$\hat{z} = -\sqrt{3}\,\hat{r}^2 + \sqrt{3}\,\hat{r}^3 \tag{22}$$

RESULTS AND DISCUSSION

In this section, results of computation by the present method are compared with experimental data and with the results of other computational methods to demonstrate the applicability of the numerically generated orthogonal coordinate system of reference 6 for flow-field calculations.

Sphere

Pressure distributions over a sphere for $\gamma = 1.4$ are presented in figure 4 for free-stream Mach numbers of 2, 3, 4, 6.05, and 8.06. Experimental data from reference 10 and computed results from reference 3 are presented for comparison. The surface pressures calculated by the present method agree well with the other results for each Mach number considered.

The shock-layer thickness for these conditions is presented in figure 5. The agreement with the other results is excellent except at $M_\infty = 2$ where the experimental data fall slightly below the calculated results. Since shock-layer thickness changes rapidly at low Mach numbers, this behavior could easily be due to a small change in the effective Mach number for the experimental tests which would change the shock-layer thickness but would have little effect on the measured pressure distribution.

The calculated shock-wave shape and sonic-line location about a sphere at $\gamma = 1.4$ are presented in figure 6 for free-stream Mach numbers of 6.8 and 4.76. Experimental data from references 11 and 12 are presented for comparison. For both conditions, the agreement with the experimental data is very good.

Paraboloid

The calculated surface pressure distributions over a paraboloid at $\gamma = 1.4$ are presented in figure 7 for Mach numbers of 3 and 10. Calculated results from references 3 and 13 are included for comparison. The results of the present calculation are in very good agreement with the other calculated results.

The shock-layer thicknesses for these conditions are compared in figure 8 where, again, excellent agreement with the results of references 3 and 13 will be noted.

Ellipsoid

Pressure distributions for an ellipsoid with $b/a = 0.5$ and $\gamma = 1.4$ are presented in figure 9 for Mach numbers of 4, 6.05, and 8.06. Experimental data from reference 10 and calculated results from reference 3 are presented for comparison. The present calculated results agree closely with the other data for each Mach number.

Pressure distributions for an ellipsoid with $b/a = 1.5$ and $\gamma = 1.4$ are presented in figure 10 for Mach numbers of 3, 4, 6.05, and 8.06. Experimental data from reference 10 and calculated results from reference 3 are presented for comparison. The present calculated results agree closely with the other data for each Mach number.

Shock-layer thickness for these conditions is presented in figure 11 for Mach numbers of 3 and 8.06. For each Mach number, the present calculated results agree closely with the other data.

The shock-wave shape and sonic-line location about an ellipsoid with $b/a = \sqrt{2}$ are presented in figure 12 for $\gamma = 1.4$ and $M_\infty = 6.8$. Experimental results from reference 11 are included for a comparison. The present computed results are in excellent agreement with the experimental results of reference 11.

Hyperboloid

The shock-wave shape and sonic-line location about a 39.37° hyperboloid at $M_\infty = 6.8$ and $\gamma = 1.4$ are compared with experimental data from reference 11 (fig. 13). The present calculated results are in very good agreement with the experimental data.

Hemisphere Cylinder

Pressure distributions on a hemisphere cylinder for $\gamma = 1.4$ are presented in figure 14 for free-stream Mach numbers of 3, 4.03, 5.06, and 6.03. Experimental results from reference 14 are presented for comparison. The calculated results are in excellent agreement with the experimental data except at the highest Mach number ($M_\infty = 6.03$) where the results tend to deviate slightly at the downstream locations. The reason for this deviation is not known; however, a similar trend was noted in reference 14.

Shock-wave shapes for these conditions are presented in figure 15 where excellent agreement with the experimental data is shown.

Spherically Blunted Cone

The calculated shock-wave shape about a spherically blunted 30° half-angle cone in helium ($\gamma = 5/3$) at $M_\infty = 20.3$ is presented in figure 16 and is compared with experimental data from reference 15. The agreement between the calculated and experimental data is excellent. The calculated drag coefficient for this case is 0.5589, which compares favorably with the measured value of 0.5540.

The next case considered is a spherically blunted, 60° half-angle cone in air ($\gamma = 1.4$) at a free-stream Mach number of 4.63. For this large half-angle cone, sonic conditions exist on the cone surface at the downstream corner. These conditions were imposed simply by fixing the corner surface pressure at the sonic value and carrying out the remainder of the calculation in the usual manner. The results for this case are presented in figures 17 and 18, along with experimental data from reference 16 for comparison. As illustrated in figure 17, the sonic line for this case extends beyond the last grid line so that the entire subsonic region is not enclosed within the computational space. Although this can lead to computational difficulties, it did not in the present case, and the results obtained are in good agreement with the experimental data. (See figs. 17 and 18.)

Reverse Curvature Body

The final case considered is a reverse curvature body with a nose shape (defined by eq. (22)) matched to a 30° conical afterbody. This is a body shape that might result from ablation in the stagnation region due to high heating rates (as, for example, on a planetary probe). The converged coordinate system associated with this configuration is shown in figure 19; the shock-wave shape and sonic-line location are shown in figure 20; and the surface pressure distribution is shown in figure 21. Since no known experimental data or theoretical results are available on this type body shape for comparison, these results are included here only to illustrate the type of complex body shape for which a flow field can be computed with the numerically generated coordinate system of reference 6. In fact, it is with this type of complex body shape that it is anticipated that the numerically generated orthogonal coordinate of reference 6 will be most useful.

It should be noted that a nonuniform spacing of grid points on the surface has been used in order to concentrate points in the expansion region near the beginning of the conical afterbody. This is a very useful feature of this coordinate system since any nonuniformity in the physical spacing of grid points is accounted for through the metric coefficients.

CONCLUDING REMARKS

A numerically generated orthogonal coordinate system (with the body surface and shock wave as opposite boundaries) has been applied with a time asymptotic method to obtain steady-flow solutions for axisymmetric inviscid flow over several blunt bodies including spheres, paraboloids, ellipsoids, hyperboloids, hemisphere cylinders, spherically blunted cones, and a body with a concavity in the stagnation region. Comparisons with experimental data and the results of other computational methods have demonstrated that accurate solutions can be obtained using this approach. The numerically generated orthogonal coordinate system used in the present paper should prove useful for applications to complex body shapes, particularly those with concave regions. In addition, the use of the present orthogonal coordinate system simplifies the form of the governing equations and simplifies the application of boundary conditions at the body surface and shock wave.

Langley Research Center
National Aeronautics and Space Administration
Hampton, VA 23665
January 22, 1980

APPENDIX

CALCULATION OF PROPERTIES AT SHOCK WAVE

A method similar to that presented in reference 9 has been used to calculate the shock velocity and other thermodynamic properties at the shock wave from the pressure. Consider the shock wave illustrated in sketch (a) which can be expressed as a function of $Z, r_s = r_s(Z)$

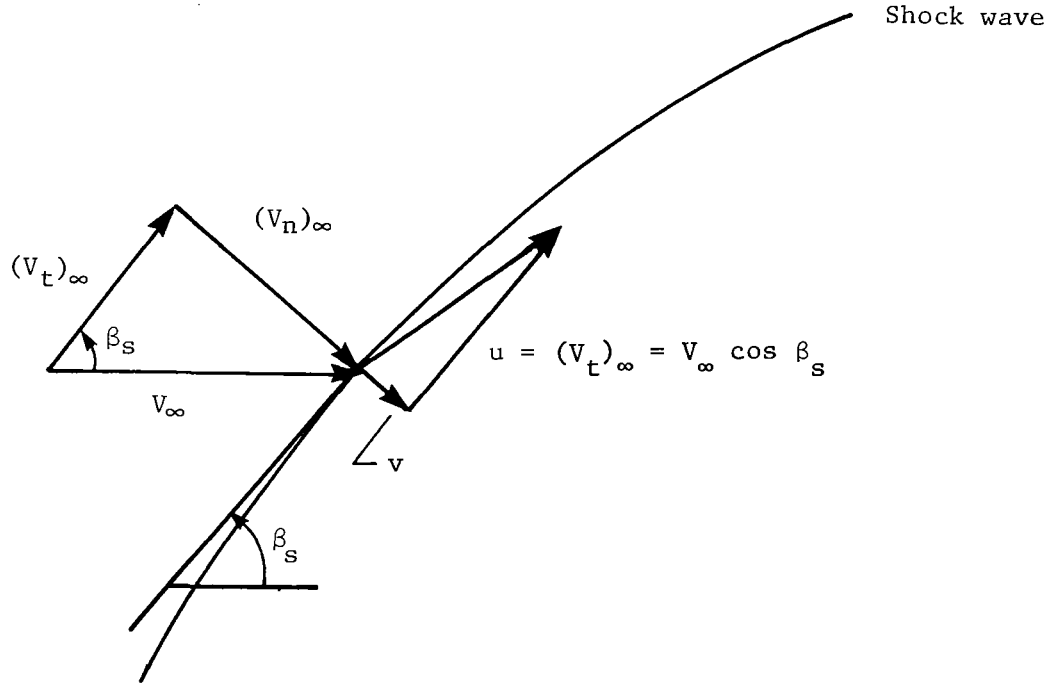

Sketch (a)

The shock-wave angle β_s is given by the equation

$$\beta_s = \tan^{-1} (dr_s/dZ) \tag{A1}$$

and the components of free-stream velocity tangent and normal to the shock wave are given, respectively, by the equations

$$(V_t)_\infty = V_\infty \cos \beta_s \tag{A2}$$

$$(V_n)_\infty = V_\infty \sin \beta_s \tag{A3}$$

APPENDIX

Changes in properties across the shock wave can be related to the normal component of free-stream velocity and the shock velocity, as illustrated in sketch (b).

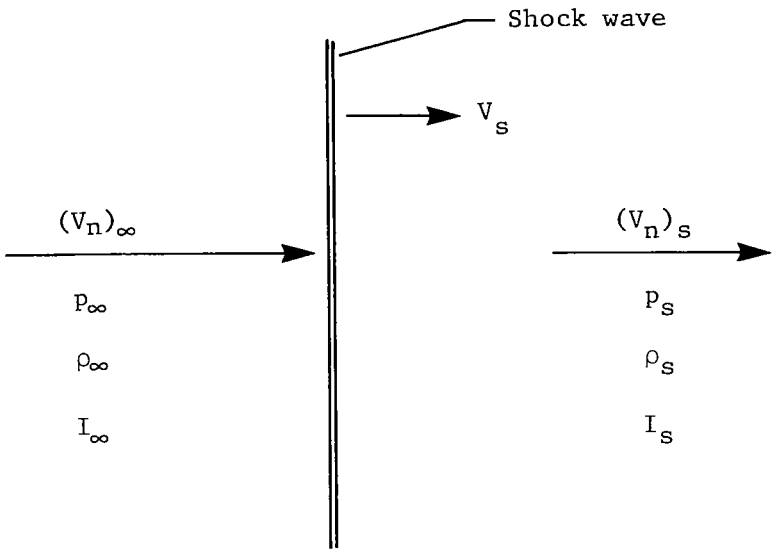

Sketch (b)

Conditions across the shock wave can be related by the following normal shock-wave equation (since $\rho_\infty = 1$):

$$(V_n)_\infty - V_s = \rho_s \left[(V_n)_s - V_s\right] \tag{A4}$$

$$p_\infty + \left[(V_n)_\infty - V_s\right]^2 = p_s + \rho_s \left[(V_n)_s - V_s\right]^2 \tag{A5}$$

$$I_\infty + \frac{\left[(V_n)_\infty - V_s\right]^2}{2} = I_s + \frac{\left[(V_n)_s - V_s\right]^2}{2} \tag{A6}$$

Now, rearranging equation (A5), the following expression can be obtained:

$$p_s - p_\infty = \left[(V_n)_\infty - V_s\right]^2 \left\{1 - \rho_s \frac{\left[(V_n)_s - V_s\right]^2}{\left[(V_n)_\infty - V_s\right]^2}\right\} \tag{A7}$$

Combining this equation with equation (A4) and solving for $\left[(V_n)_\infty - V_s\right]^2$, the following result is obtained

$$\left[(V_n)_\infty - V_s\right]^2 = \frac{p_s - p_\infty}{1 - \frac{1}{\rho_s}} \tag{A8}$$

Similarly equation (A6) becomes

$$I_s = I_\infty + \frac{1}{2}\left[(V_n)_\infty - V_s\right]^2 \left[\left(1 - \frac{1}{\rho_s}\right)\right]^2 \tag{A9}$$

Equations (A8) and (A9) can be combined with the ideal gas equation of state $p = \rho\left(\frac{\gamma - 1}{\gamma}\right)I$ to yield the following result:

$$\frac{1}{\rho_s} = \frac{I_\infty + \frac{1}{2}(p_s - p_\infty)}{p_s\left(\frac{\gamma}{\gamma - 1}\right) - \frac{1}{2}(p_s - p_\infty)} \tag{A10}$$

Using this result, equation (A8) can be solved for the shock velocity V_s

$$V_s = (V_n)_\infty - \sqrt{\frac{p_s - p_\infty}{1 - \frac{1}{\rho_s}}} \tag{A11}$$

Using equation (A4), $(V_n)_s$ is obtained

$$(V_n)_s = \frac{1}{\rho_s}\left[(V_n)_\infty - V_s\right] + V_s \tag{A12}$$

Thus, the components of velocity downstream of the shock wave are simply

$$u = (V_t)_\infty = V_\infty \cos \beta_s \tag{A13}$$

$$v = (V_n)_s \tag{A14}$$

since the shock wave is the outer boundary of an orthogonal coordinate system.

REFERENCES

1. Moretti, Gino; and Abbett, Michael: A Time-Dependent Computational Method for Blunt Body Flows. AIAA J., vol. 4, no. 12, Dec. 1966, pp. 2136-2141.

2. Barnwell, Richard W.: Time-Dependent Numerical Method for Treating Complicated Blunt-Body Flow Fields. Analytical Methods in Aircraft Aerodynamics, NASA SP-228, 1970, pp. 177-195.

3. Hamilton, H. Harris, II: Solution of Axisymmetric and Two-Dimensional Inviscid Flow Over Blunt Bodies by the Method of Lines. NASA TP-1154, 1978.

4. Rakich, John V.; Vigneron, Yvon C.; and Tannehill, John C.: Navier-Stokes Calculations for Laminar and Turbulent Hypersonic Flow Over Indented Nosetips. AIAA Paper 78-260, Jan. 1978.

5. Graves, Randolph Anderson, Jr.: Solutions to the Navier-Stokes Equations for Supersonic Flow Over Blunt Bodies With Massive Wall Blowing. Ph. D. Diss., The George Washington Univ., 1977.

6. Graves, Randolph A., Jr.: Application of a Numerical Orthogonal Coordinate Generator to Axisymmetric Blunt Bodies. NASA TM-80131, 1979.

7. Brailovskaya, I. Yu.: A Difference Scheme for Numerical Solution of the Two-Dimensional, Nonstationary Navier-Stokes Equations for a Compressible Gas. Sov. Phys. - Doklady, vol. 10, no. 2, Aug. 1965, pp. 107-110.

8. Gnoffo, Peter A.: Forebody and Afterbody Solutions of the Navier-Stokes Equations for Supersonic Flow Over Blunt Bodies in a Generalized Orthogonal Coordinate System. NASA TP-1075, 1978.

9. Weilmuenster, K. James; and Hamilton, H. Harris, II: A Hybridized Method for Computing High Reynolds-Number Hypersonic Flow About Blunt Bodies. NASA TP-1497, 1979.

10. Belotserkovskiy, O. M., ed.: Supersonic Gas Flow Around Blunt Bodies - Theoretical and Experimental Investigations. NASA TT F-453, 1967.

11. Osborne, W. K.; and Crane, J. F. W.: Flow Field and Pressure Distribution Measurements on Blunt-Nosed Bodies at M = 6.8: Parts I and II. C.P. No. 615, British A.R.C., 1962.

12. Kendall, James M., Jr.: Experiments on Supersonic Blunt-Body Flows. Progr. Rep. No. 20-372 (Contract No. DA-04-495-Ord 18), Jet Propulsion Lab., California Inst. Technol., Feb. 27, 1959.

13. Van Dyke, Milton D.; and Gordon, Helen D.: Supersonic Flow Past a Family of Blunt Axisymmetric Bodies. NASA TR R-1, 1959.

14. Inouye, Mamoru; and Lomax, Harvard: Comparison of Experimental and Numerical Results for the Flow of a Perfect Gas About Blunt-Nosed Bodies. NASA TN D-1426, 1962.

15. Calloway, Robert L.; and White, Nancy H.: Measured and Predicted Shock Shapes and Aerodynamic Coefficients for Blunted Cones at Incidence in Helium at Mach 20.3. NASA TP-1395, 1979.

16. Stallings, Robert L., Jr.; and Tudor, Dorothy H.: Experimental Pressure Distributions on a 120° Cone at Mach Numbers From 2.96 to 4.63 and Angles of Attack From 0° to 20°. NASA TN D-5054, 1969.

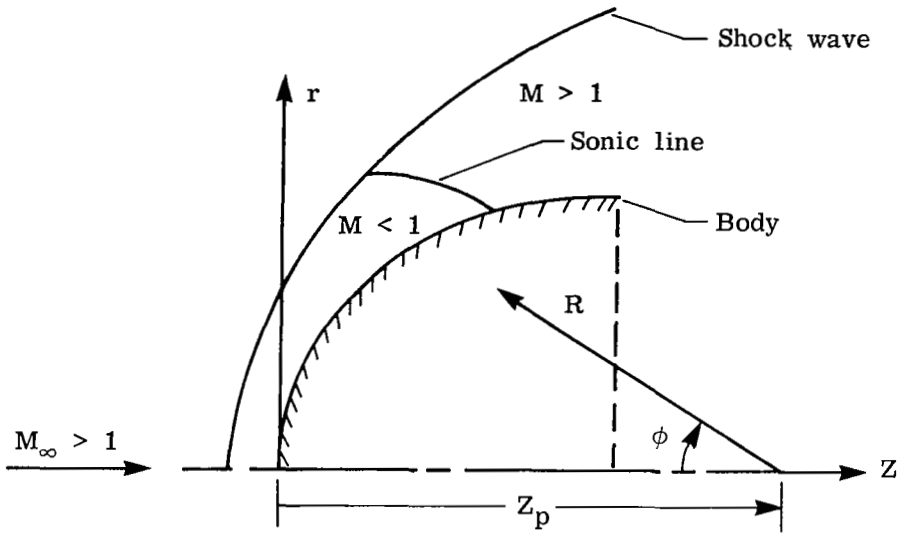

Figure 1.- Cartesian coordinate system.

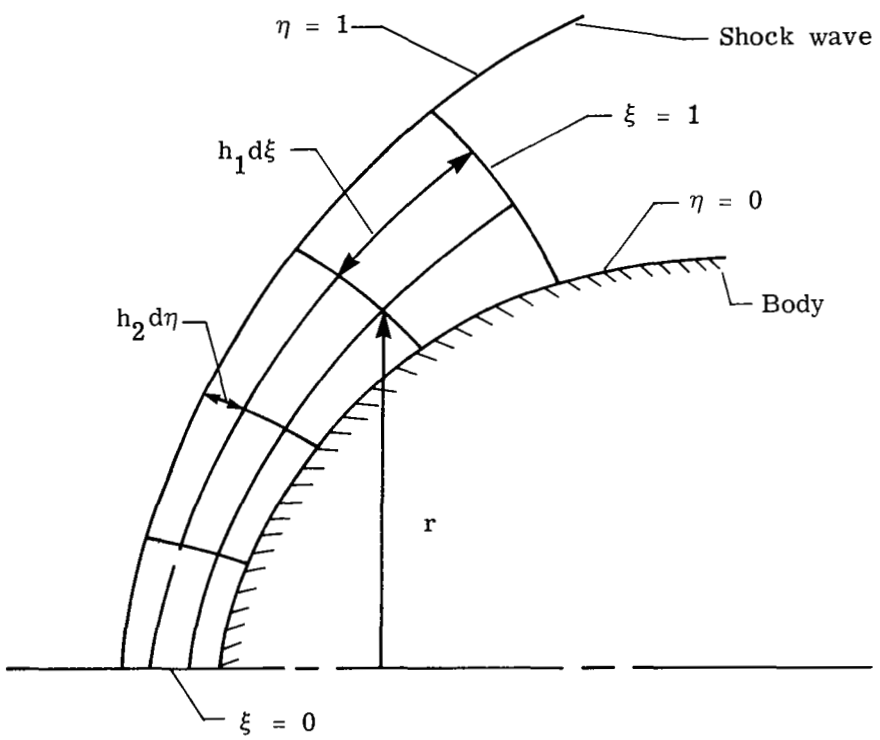

Figure 2.- Orthogonal coordinate system in physical space.

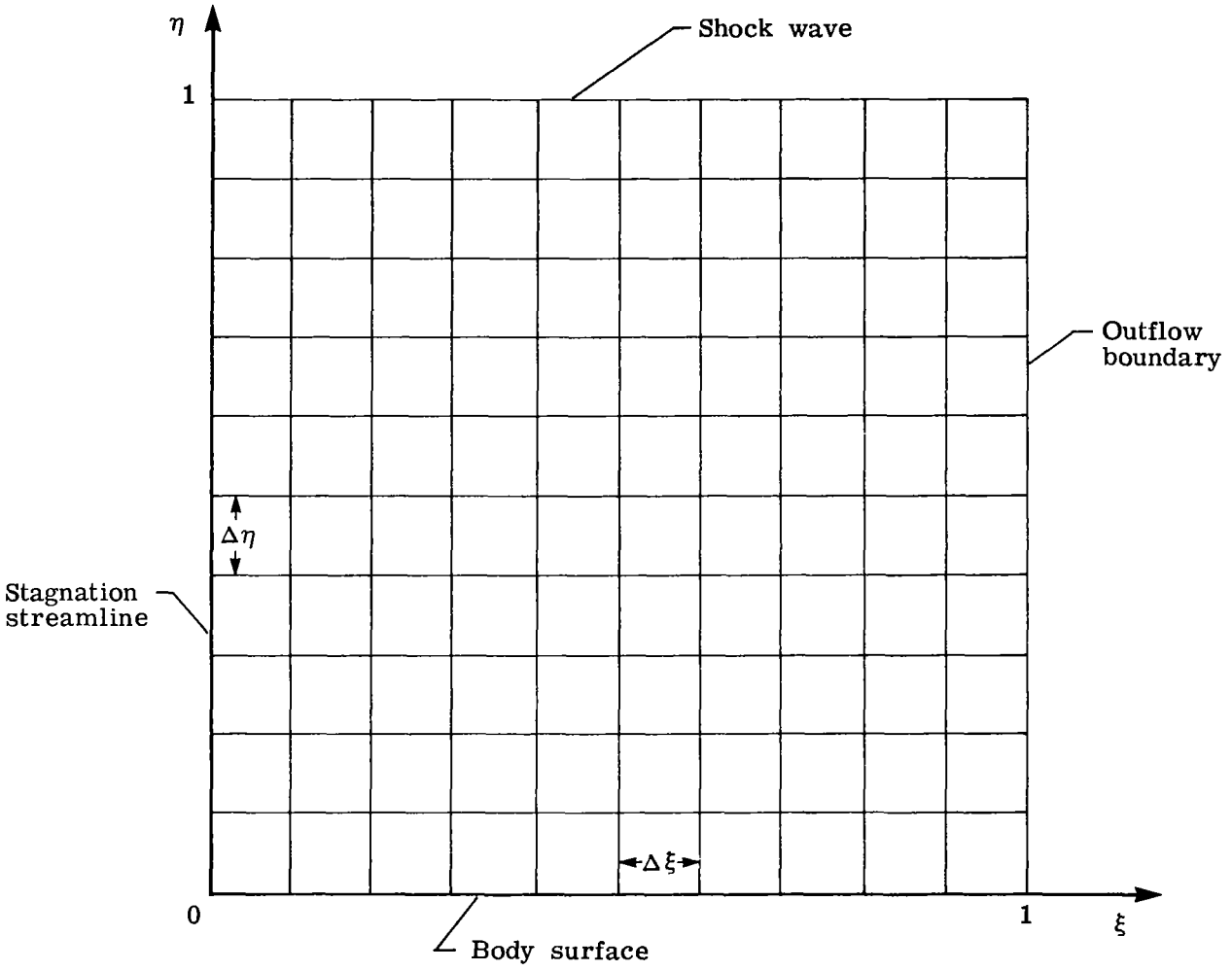

Figure 3.- Orthogonal coordinate system in computational plane.

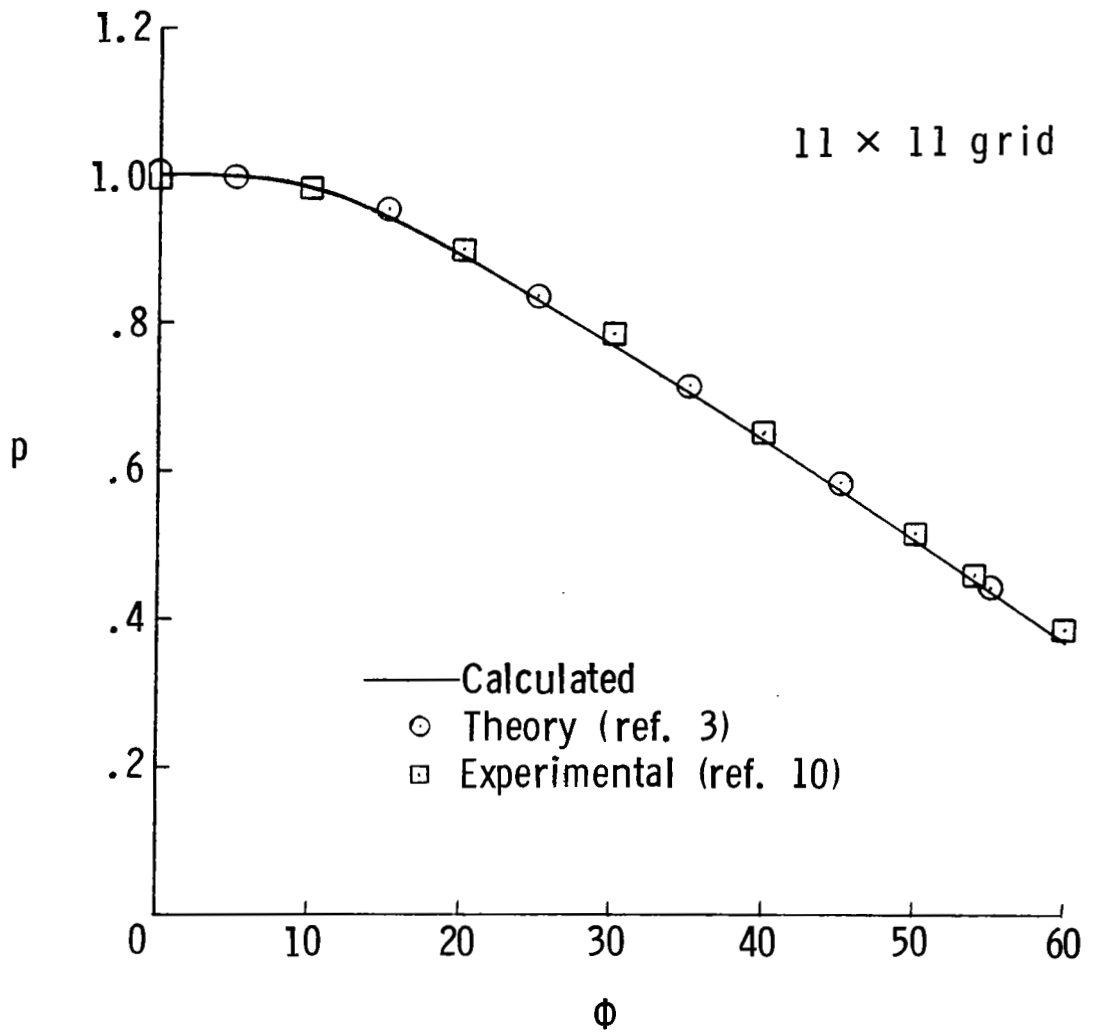

(a) $M_\infty = 2.$

Figure 4.- Pressure distribution on sphere. $z_p/R_b = 1.0$; $\gamma = 1.4$.

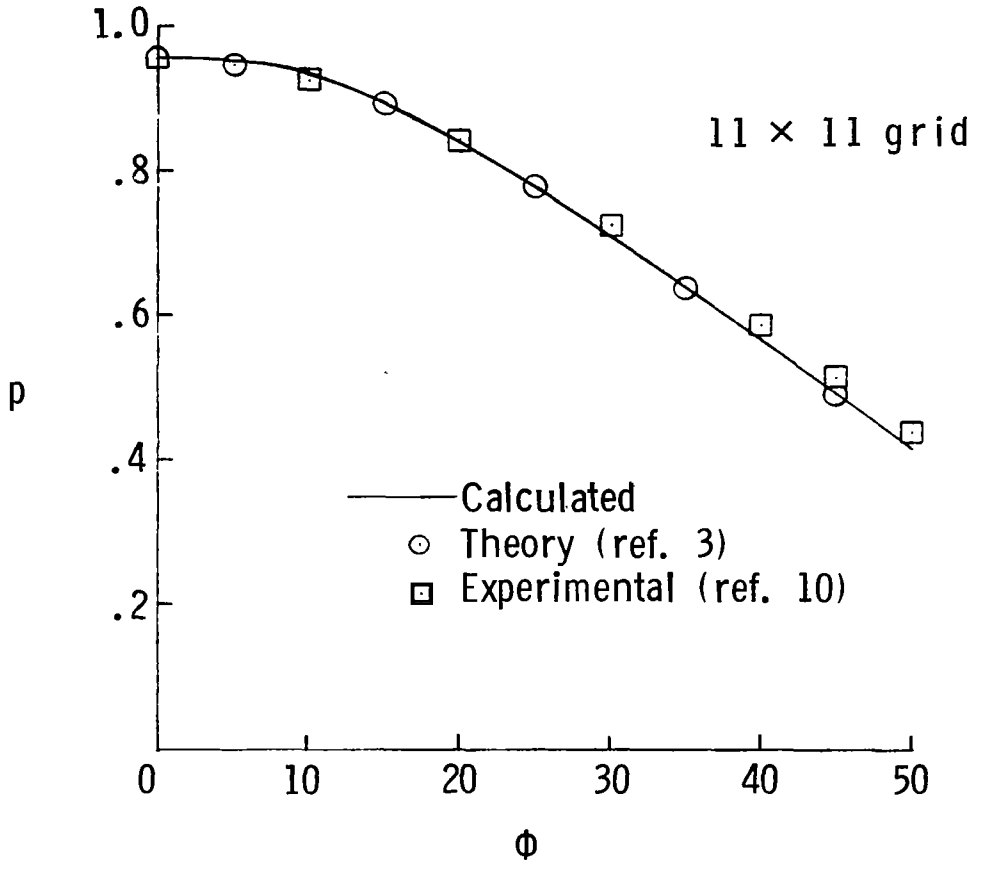

(b) $M_\infty = 3.$

Figure 4.- Continued.

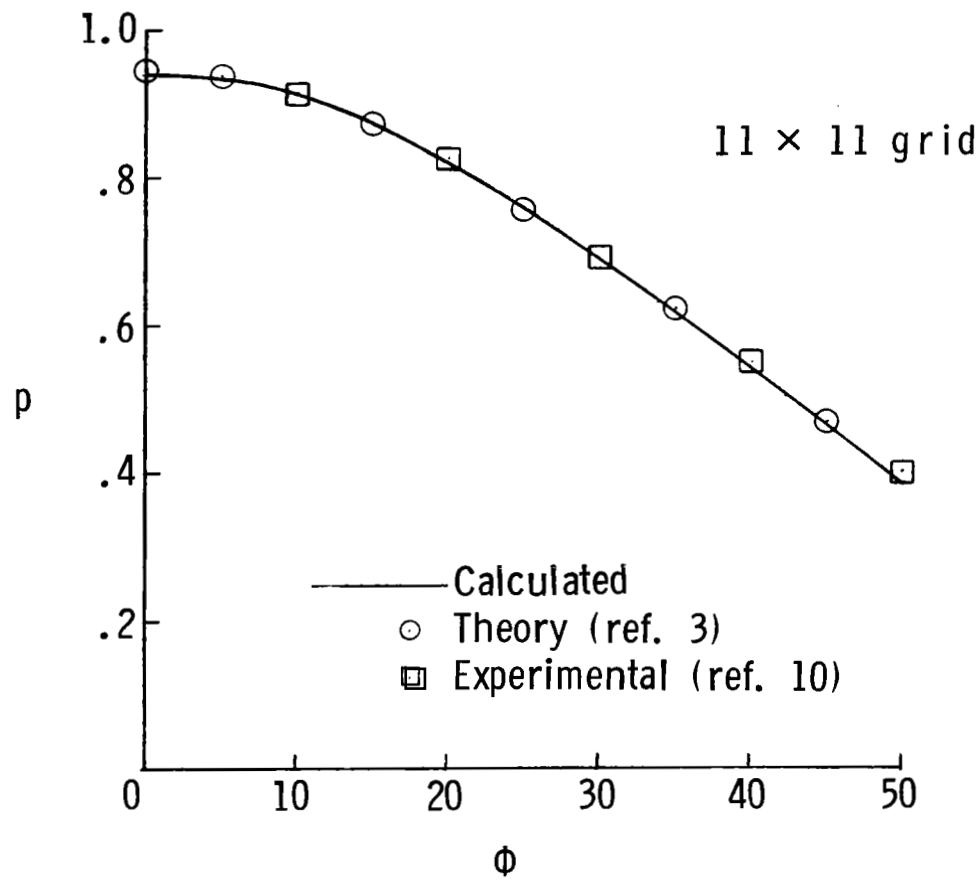

(c) $M_\infty = 4.$

Figure 4.- Continued.

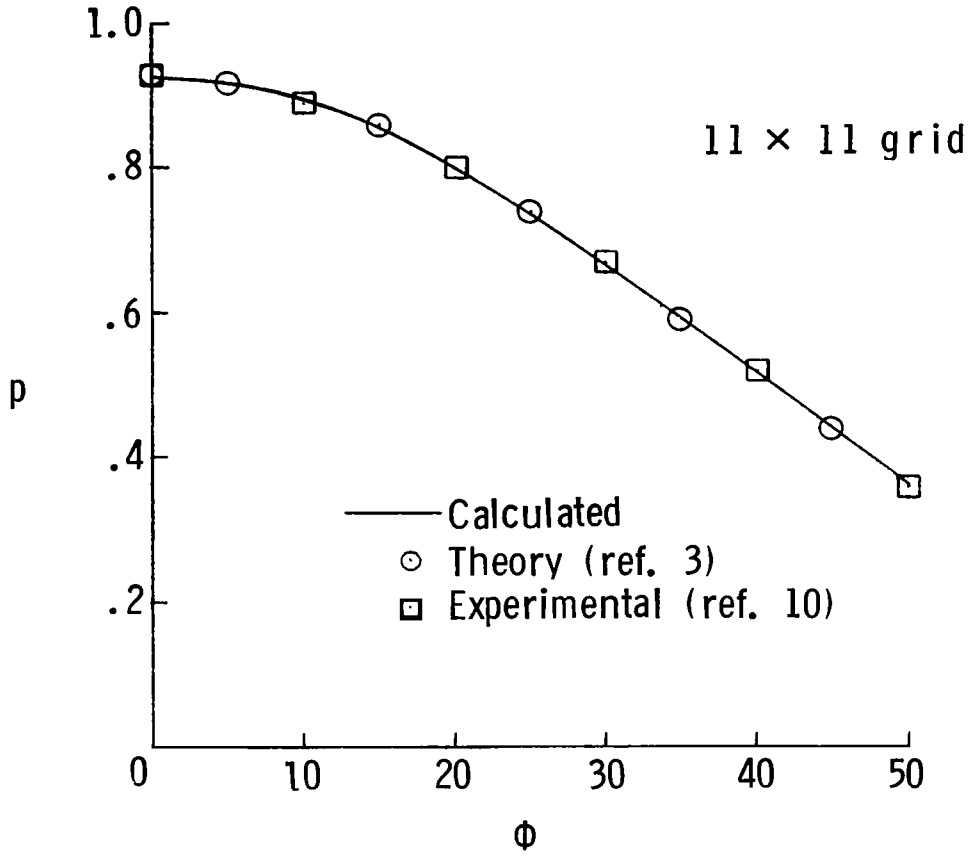

(d) $M_\infty = 6.05$.

Figure 4.- Continued.

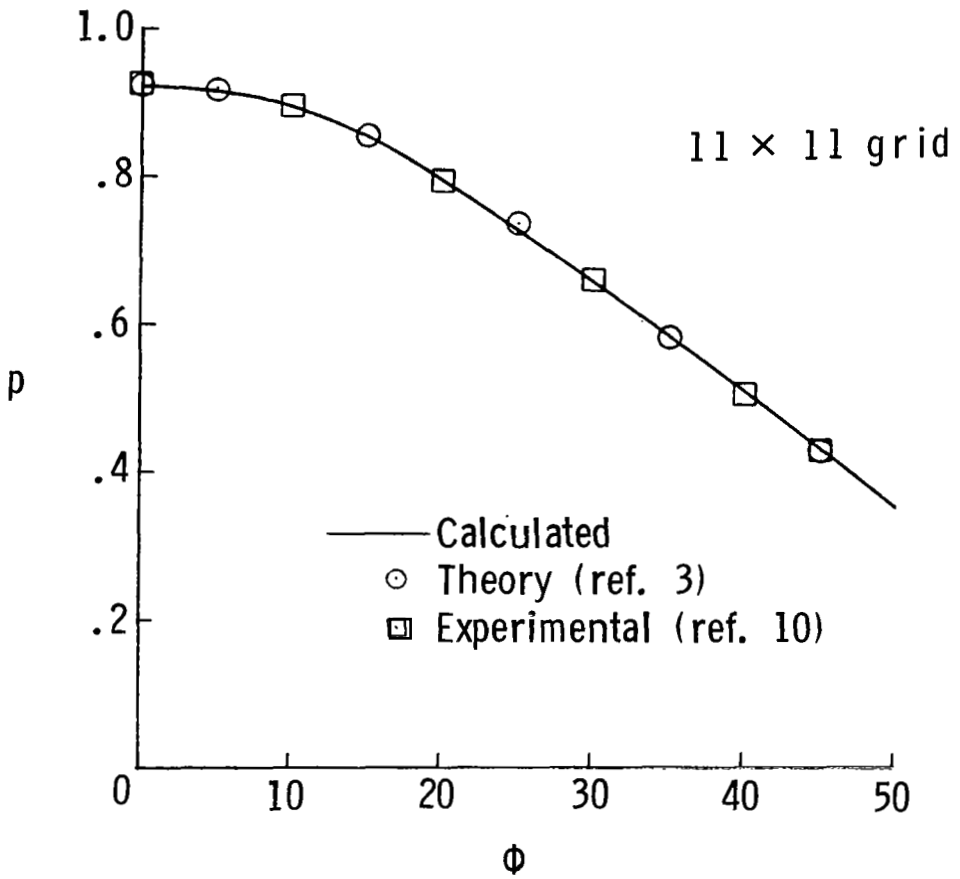

(e) $M_\infty = 8.06$.

Figure 4.- Concluded.

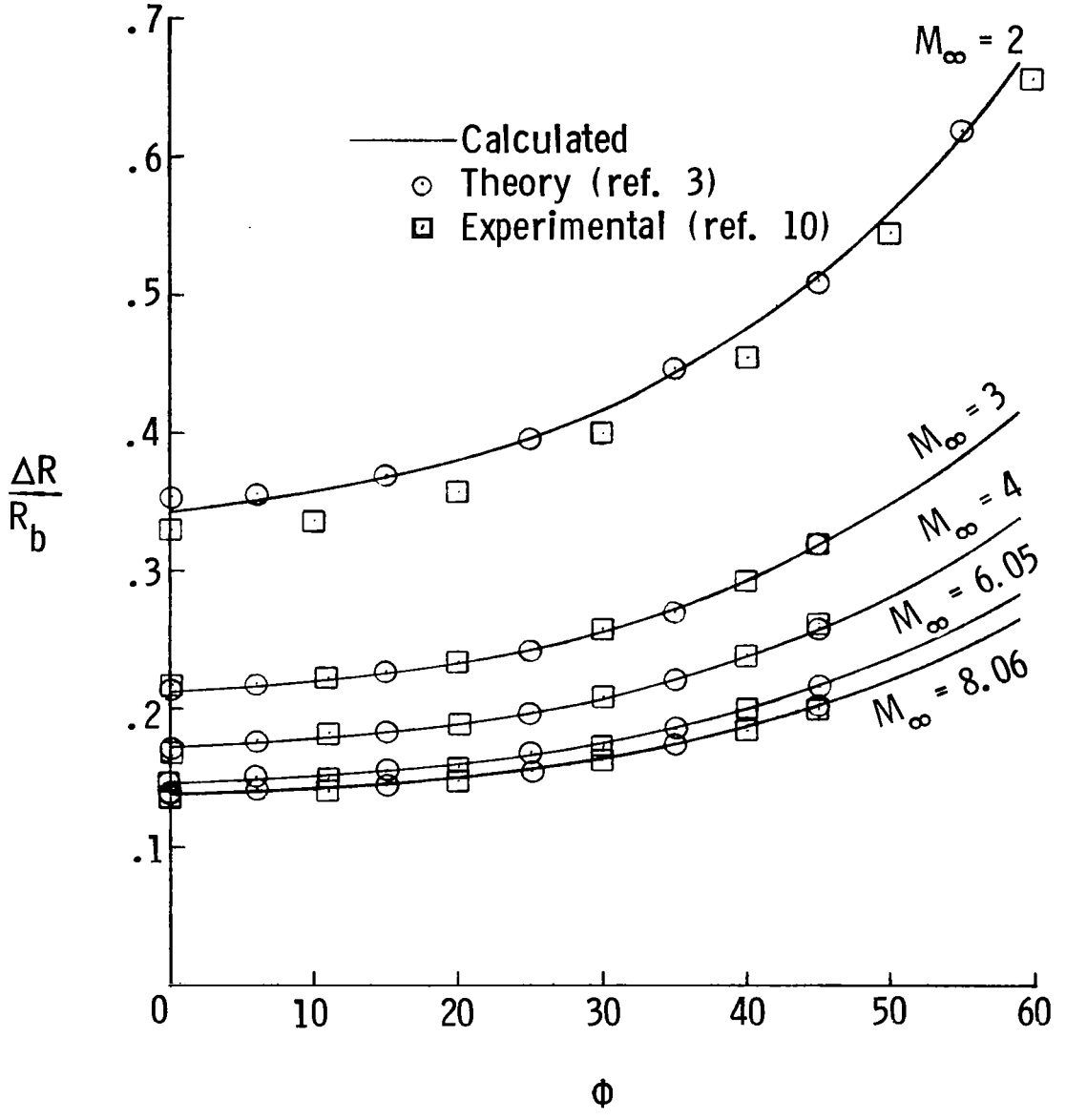

Figure 5.- Shock-layer thicknesses for sphere. $z_p/R_b = 1.0$; $\gamma = 1.4$.

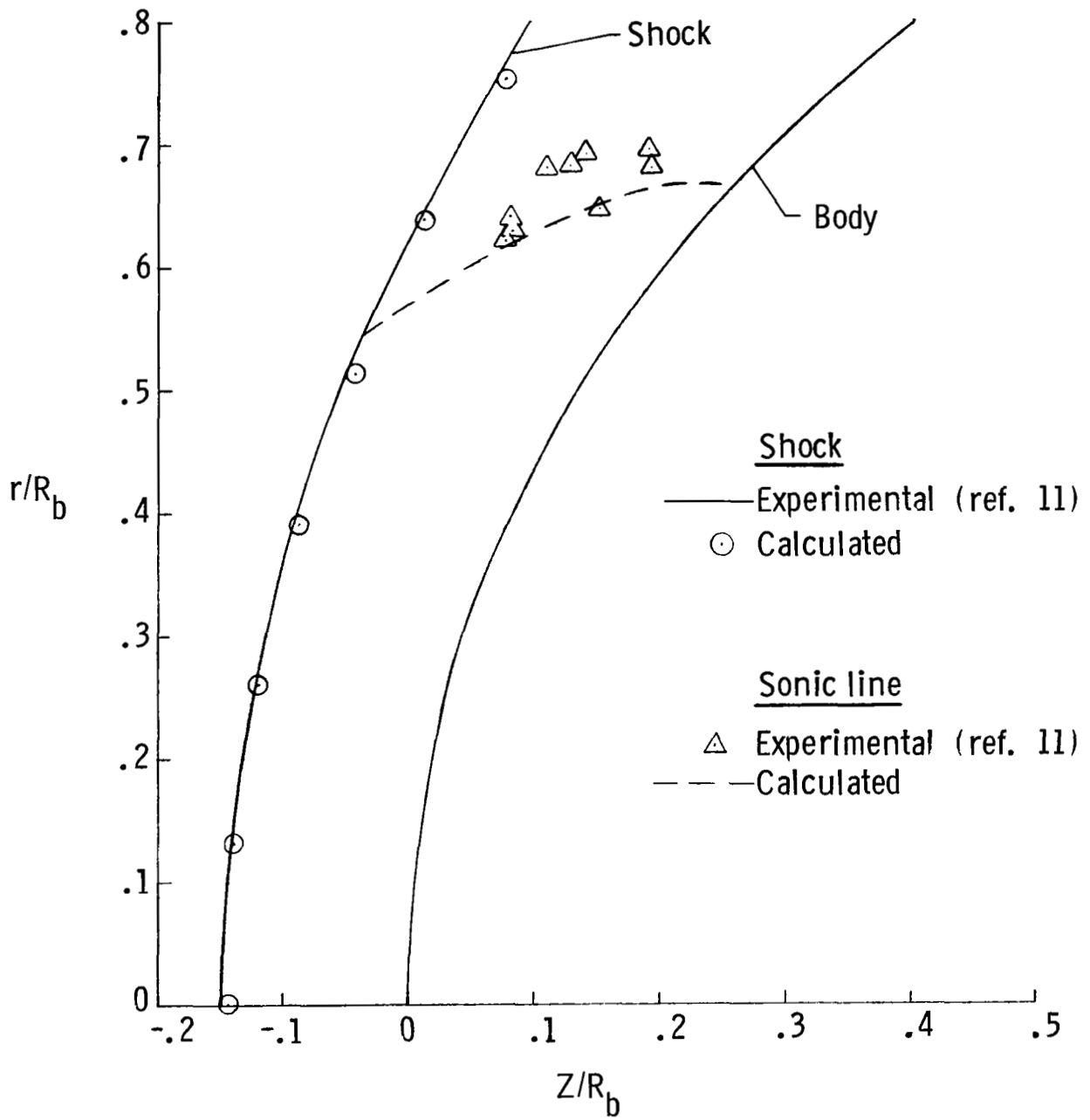

(a) $M_\infty = 6.8$.

Figure 6.- Shock-wave shape and sonic-line location for sphere. $\gamma = 1.4$.

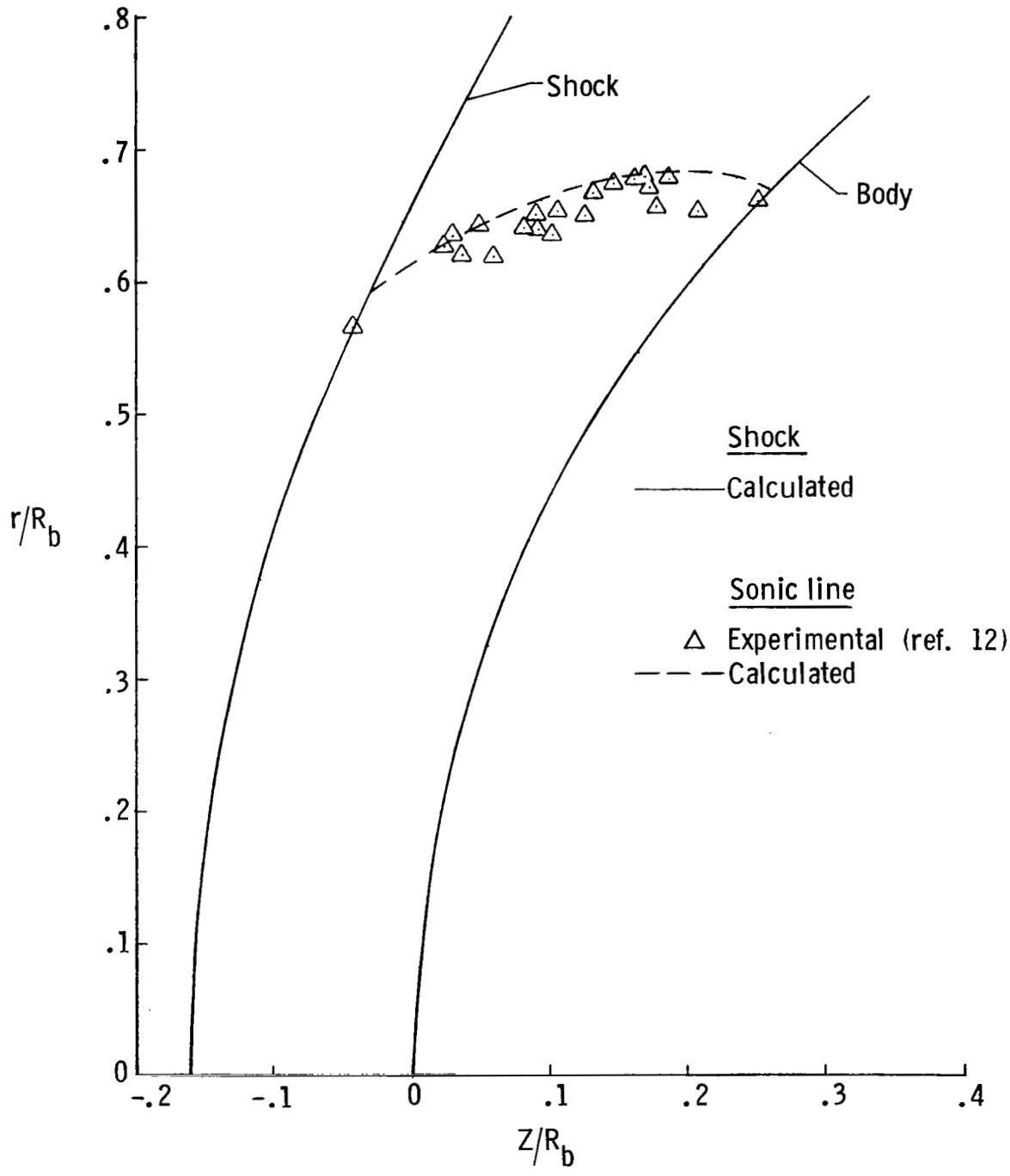

(b) $M_\infty = 4.76$.

Figure 6.- Concluded.

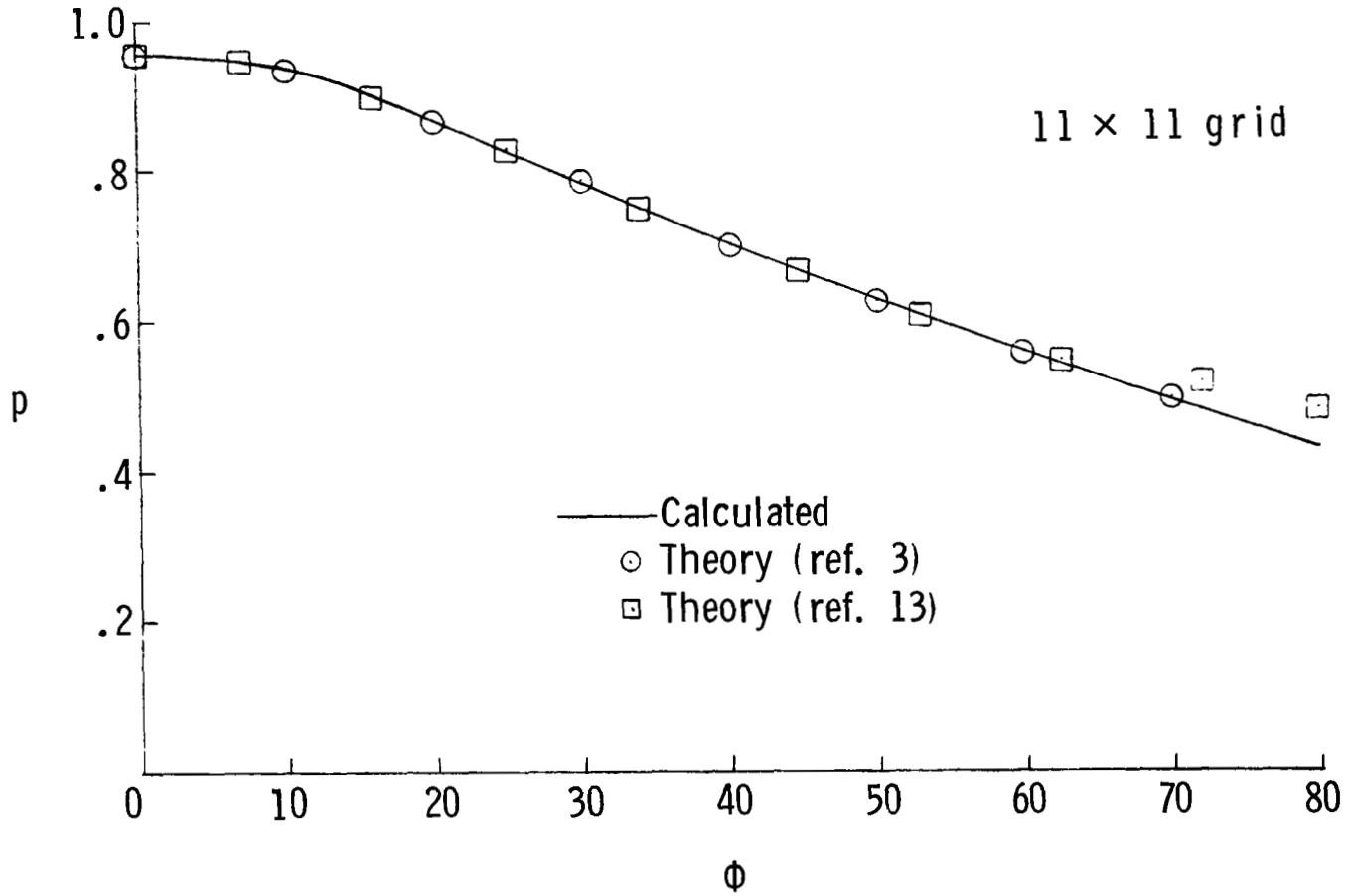

(a) $M_\infty = 3.$

Figure 7.- Pressure distribution on a paraboloid.
$Z_p/R_b = 1.0$; $\gamma = 1.4$.

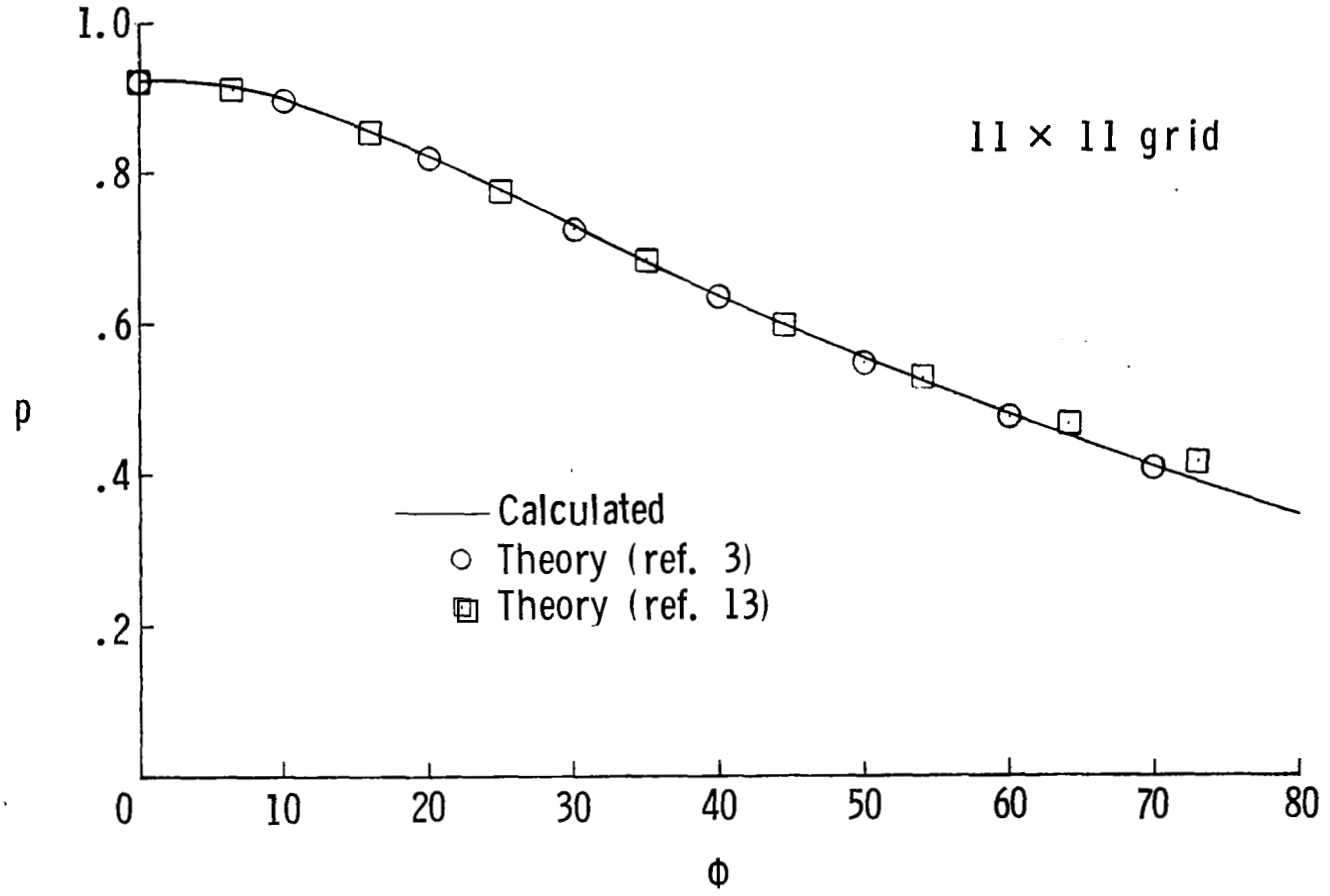

(b) $M_\infty = 10.$

Figure 7.- Concluded.

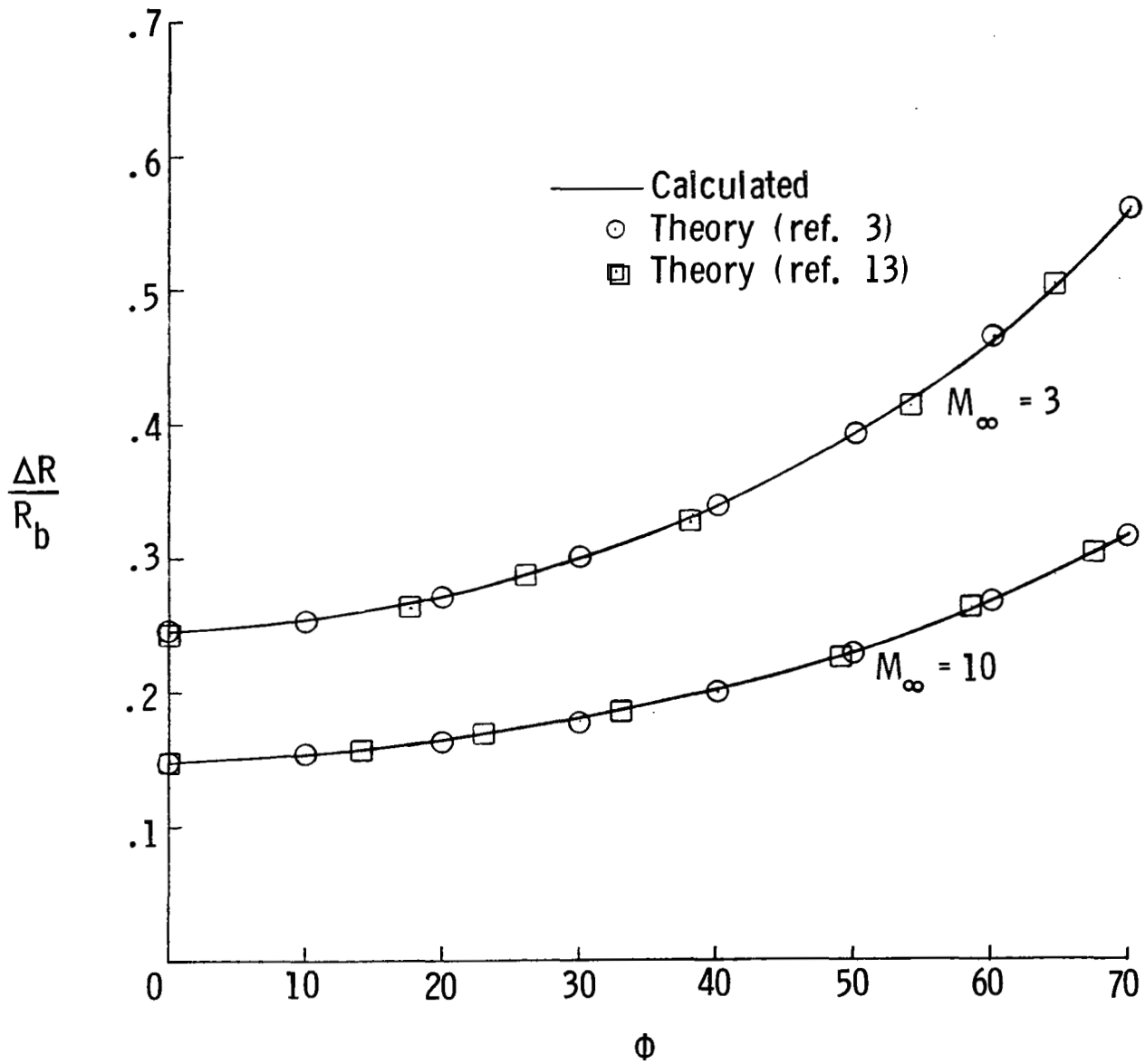

Figure 8.- Shock-layer thickness for paraboloid.
$z_p/R_b = 1.0$; $\gamma = 1.4$.

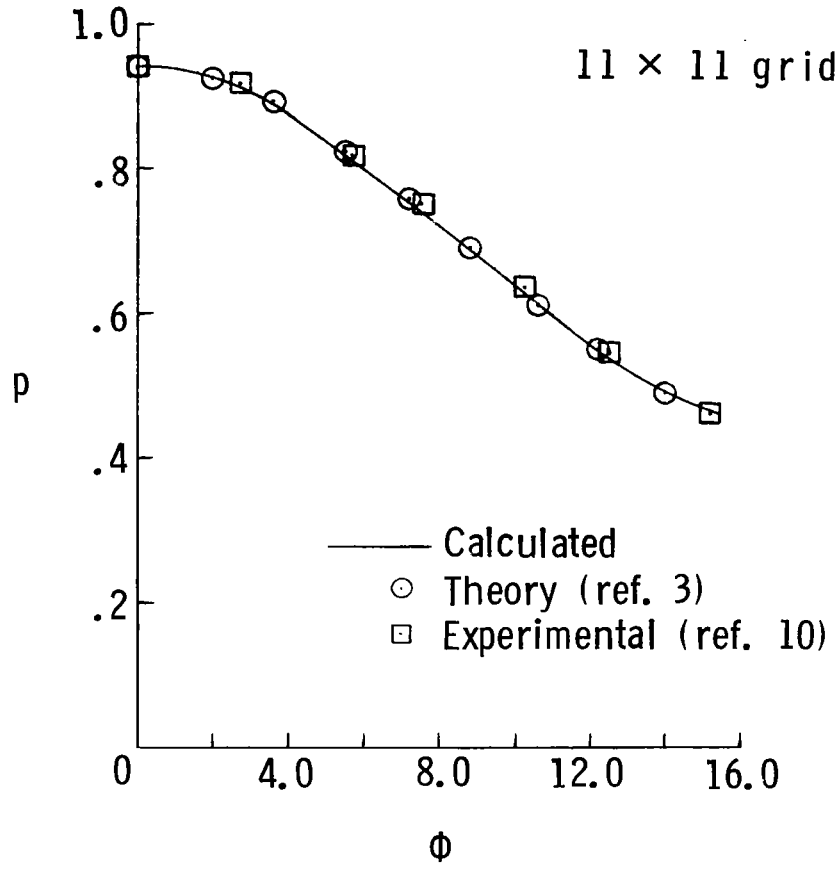

(a) $M_\infty = 4.$

Figure 9.- Pressure distribution on ellipsoid. b/a = 0.5; $z_p/R_b = 4$; $\gamma = 1.4$.

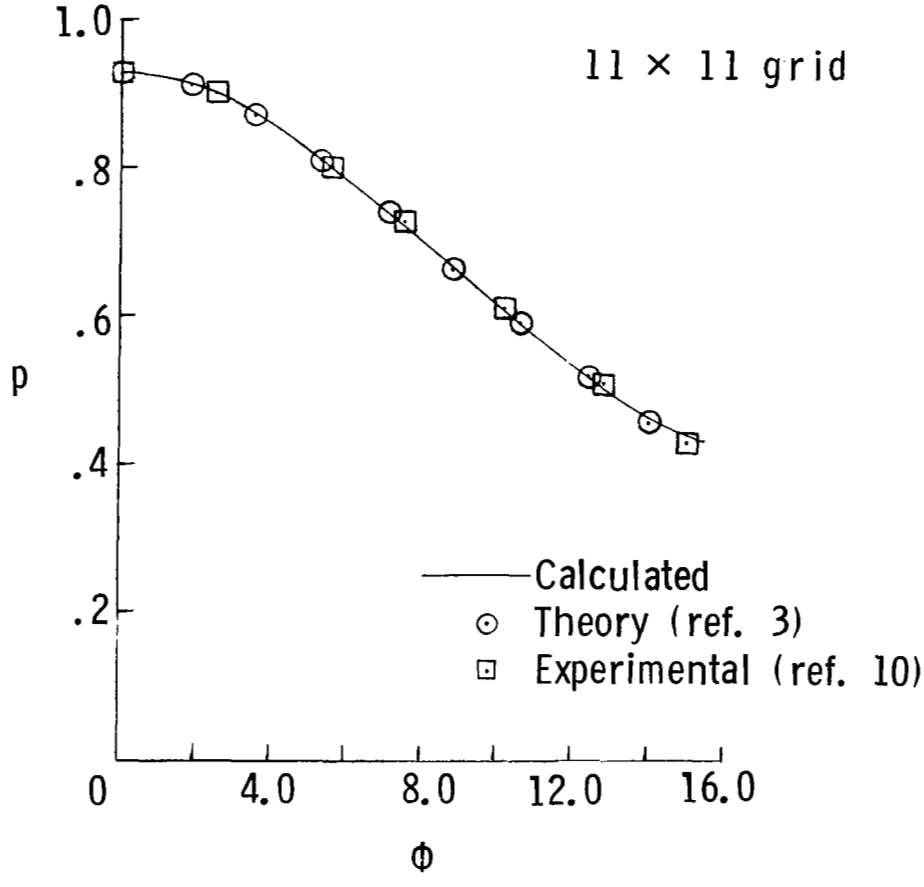

(b) $M_\infty = 6.05$.

Figure 9.- Continued.

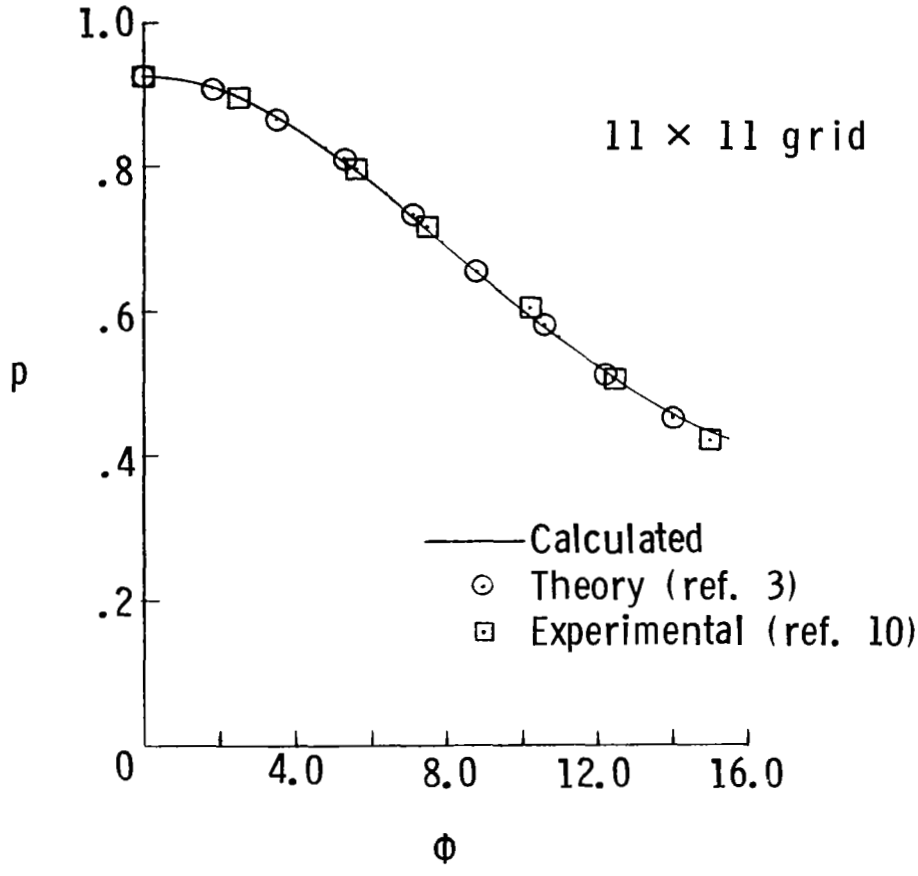

(c) $M_\infty = 8.06$.

Figure 9.- Concluded.

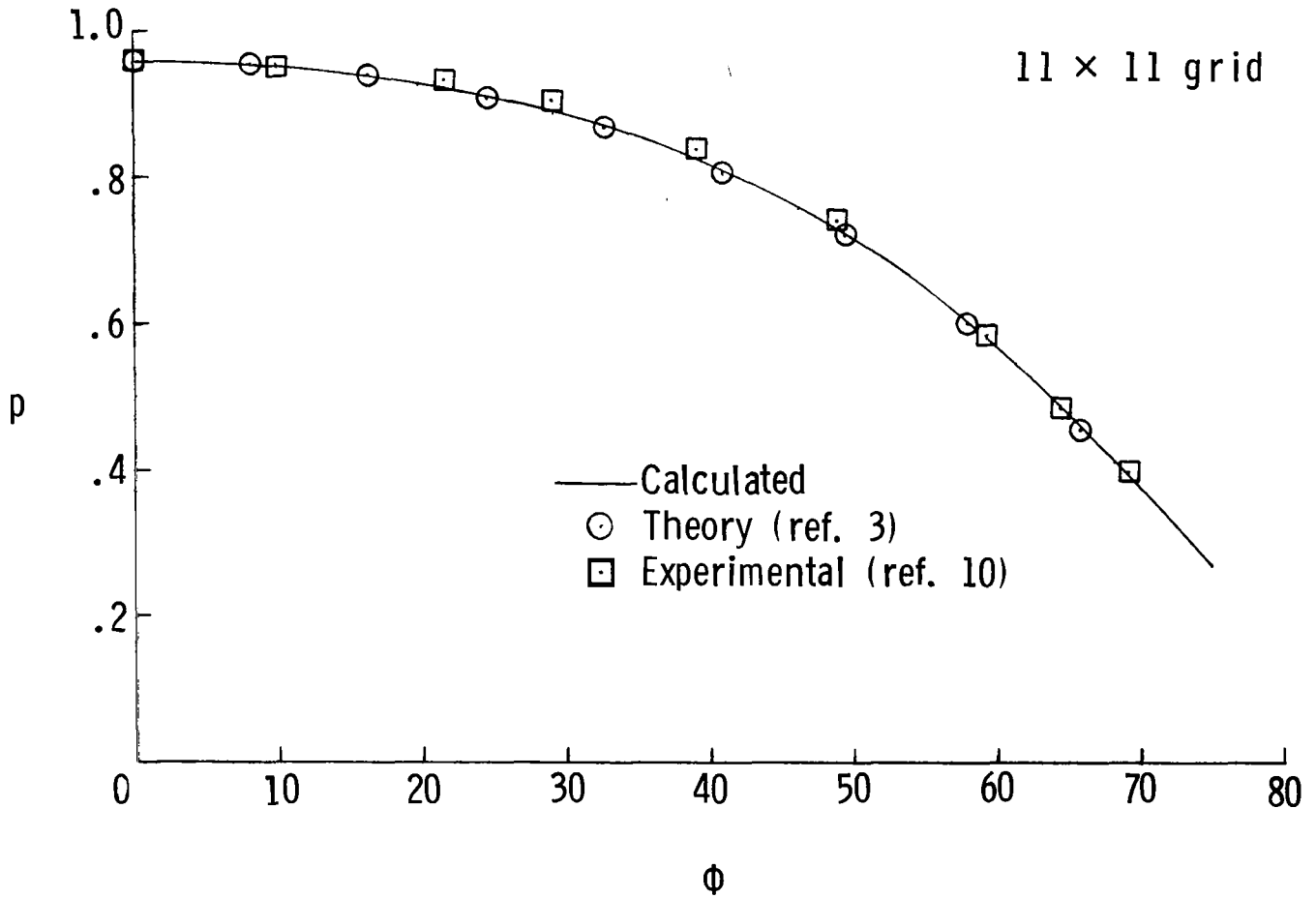

(a) $M_\infty = 3.$

Figure 10.- Pressure distribution on ellipsoid. b/a = 1.5; $z_p/R_b = 0.444$; $\gamma = 1.4$.

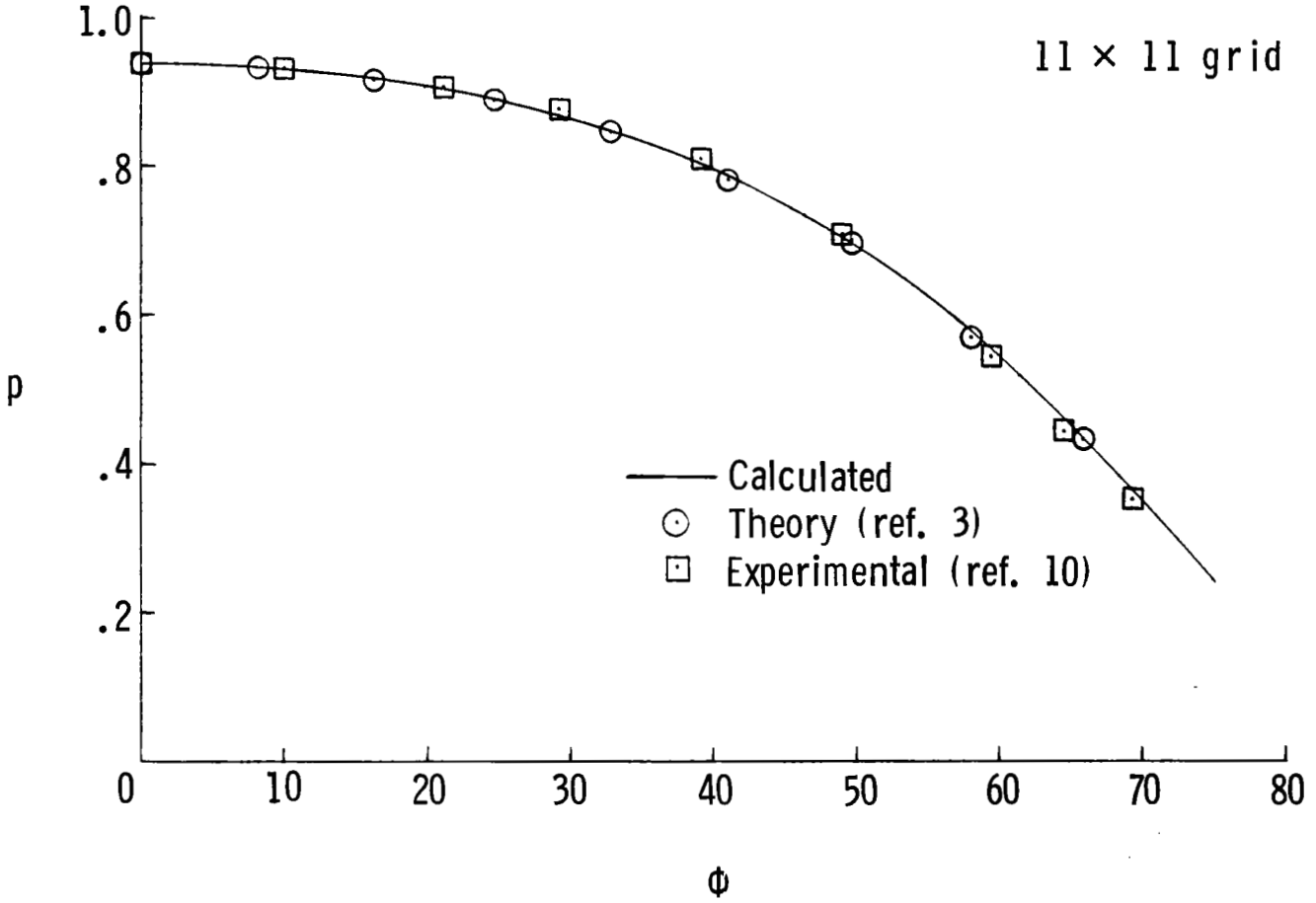

(b) $M_\infty = 4.$

Figure 10.- Continued.

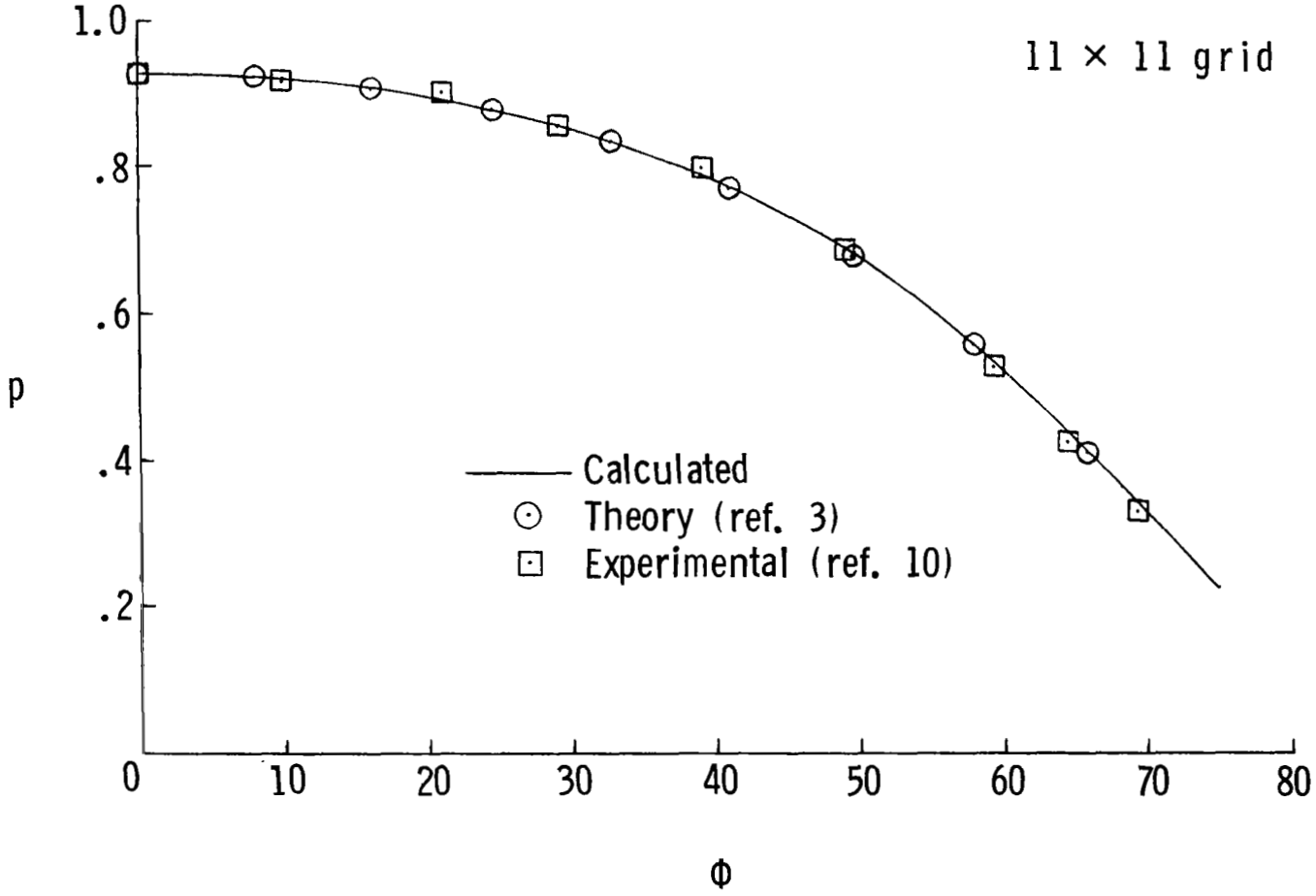

(c) $M_\infty = 6.05$.

Figure 10.- Continued.

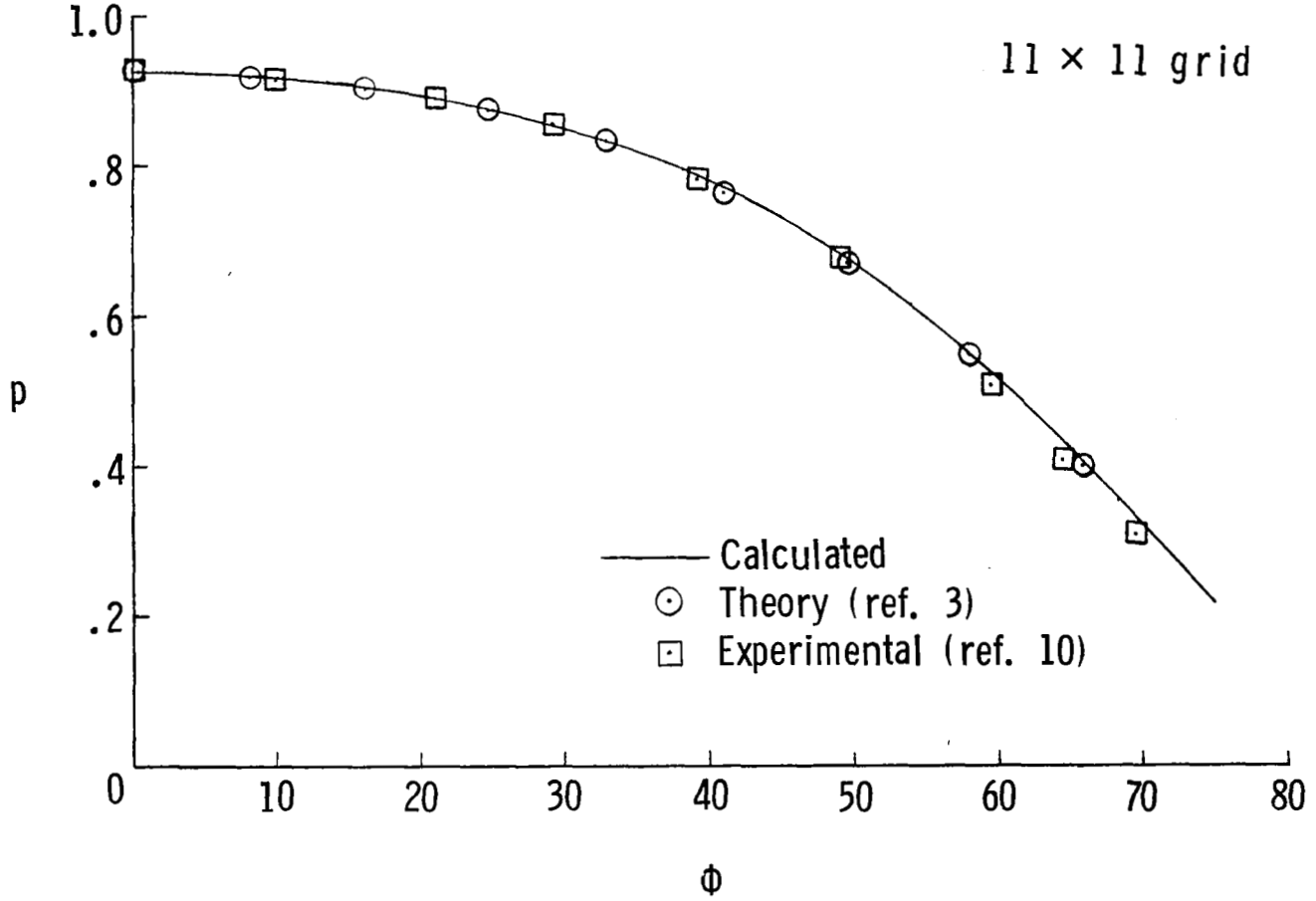

(d) $M_\infty = 8.06$.

Figure 10.- Concluded.

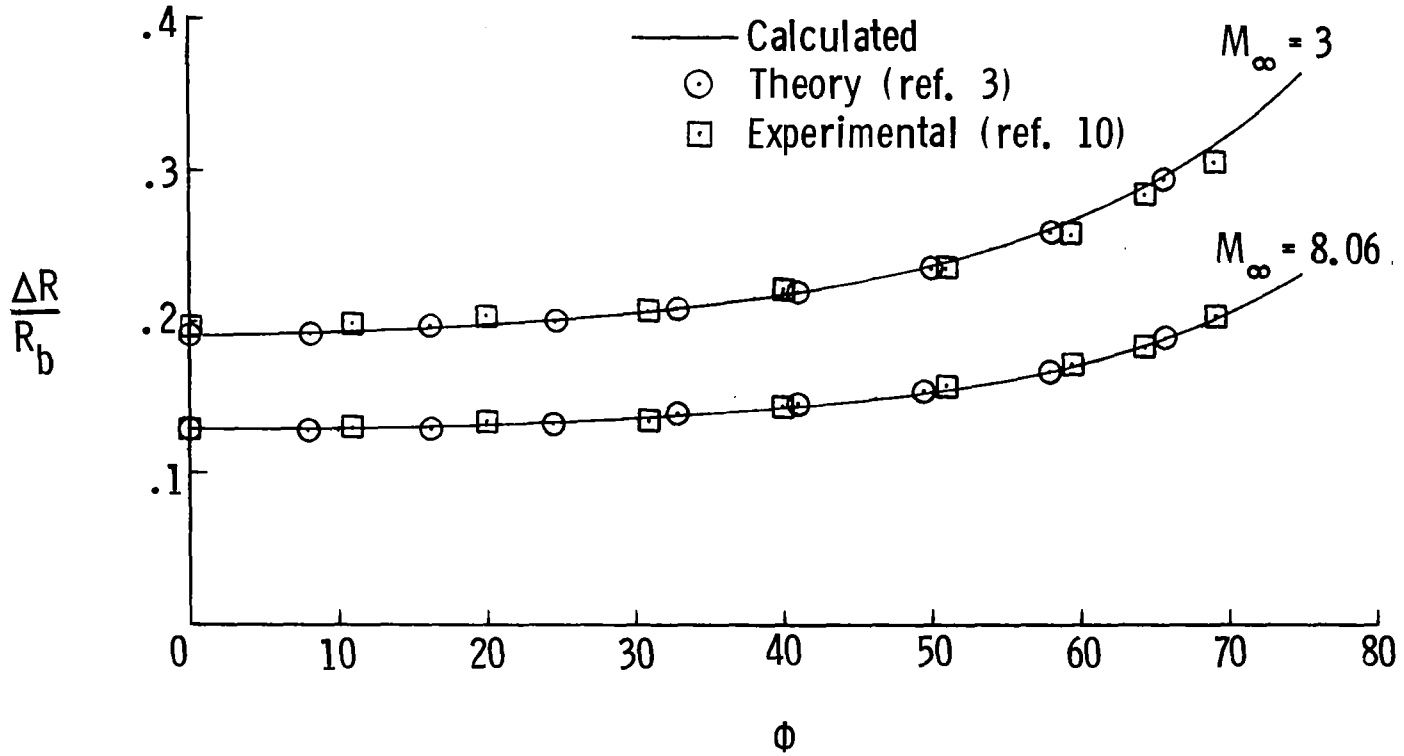

Figure 11.- Shock-layer thicknesses for ellipsoid. b/a = 1.5; $z_p/R_b = 0.444$; $\gamma = 1.4$.

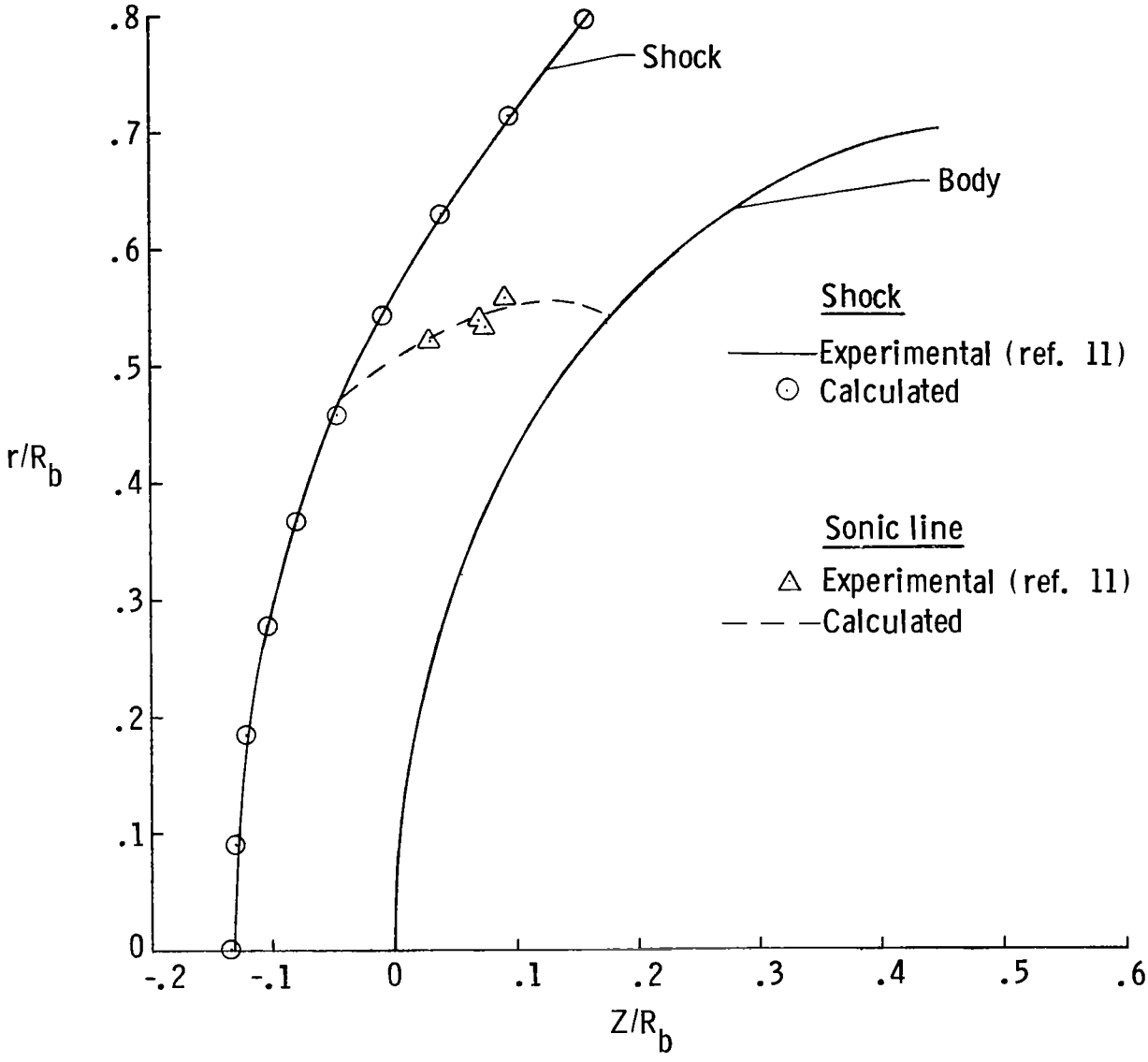

Figure 12.- Shock-wave shape and sonic-line location for ellipsoid. $b/a = \sqrt{2}$; $M_\infty = 6.8$; $\gamma = 1.4$.

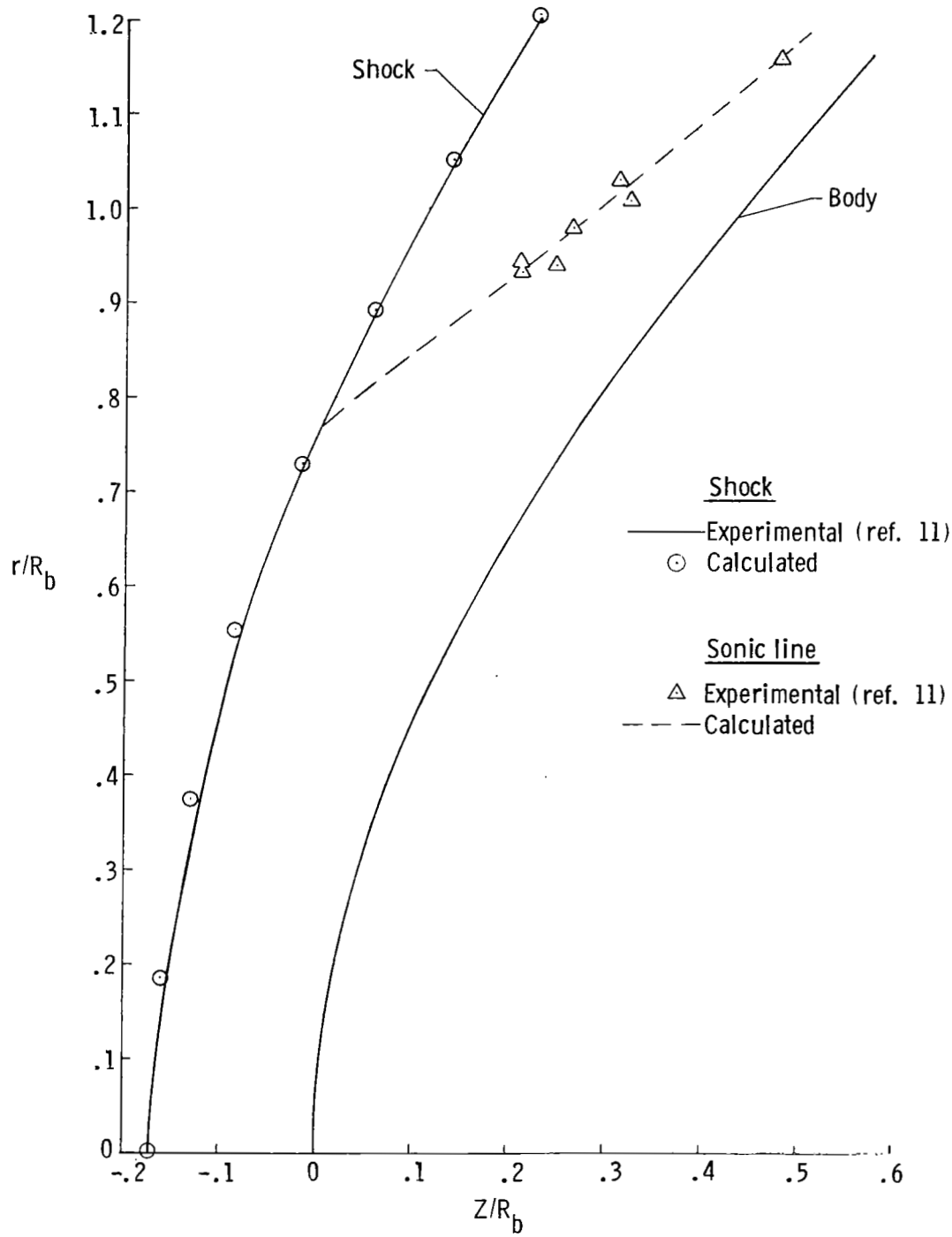

Figure 13.- Shock-wave shape and sonic-line location for 39.37° hyperboloid. $M_\infty = 6.8$; $\gamma = 1.4$.

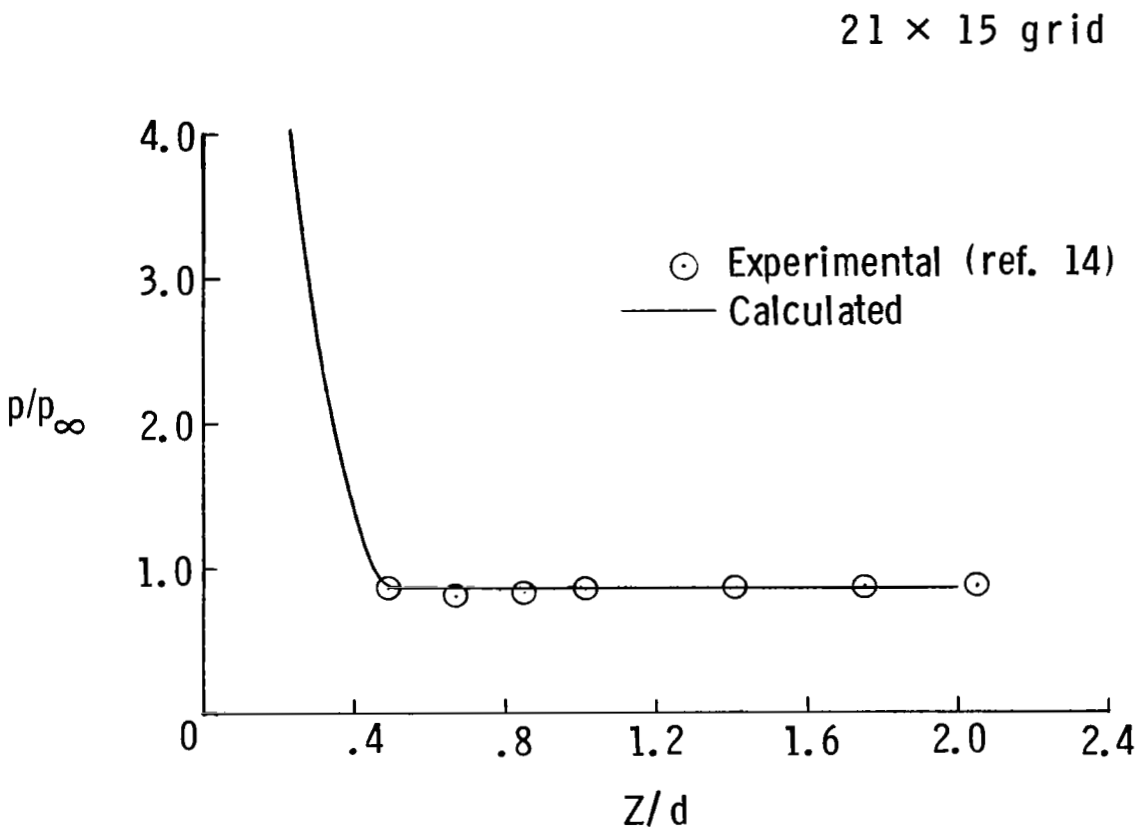

(a) $M_\infty = 3.$

Figure 14.- Pressure distribution on hemisphere-cylinder. $\gamma = 1.4$.

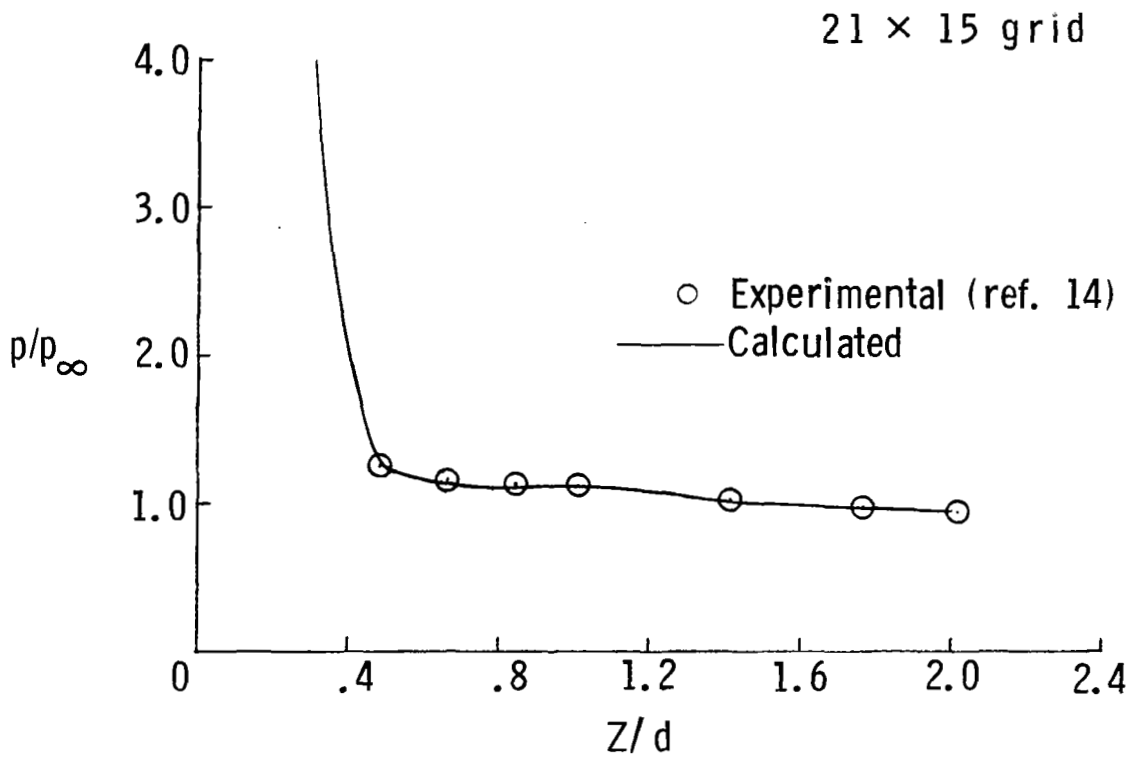

(b) $M_\infty = 4.03$.

Figure 14.- Continued.

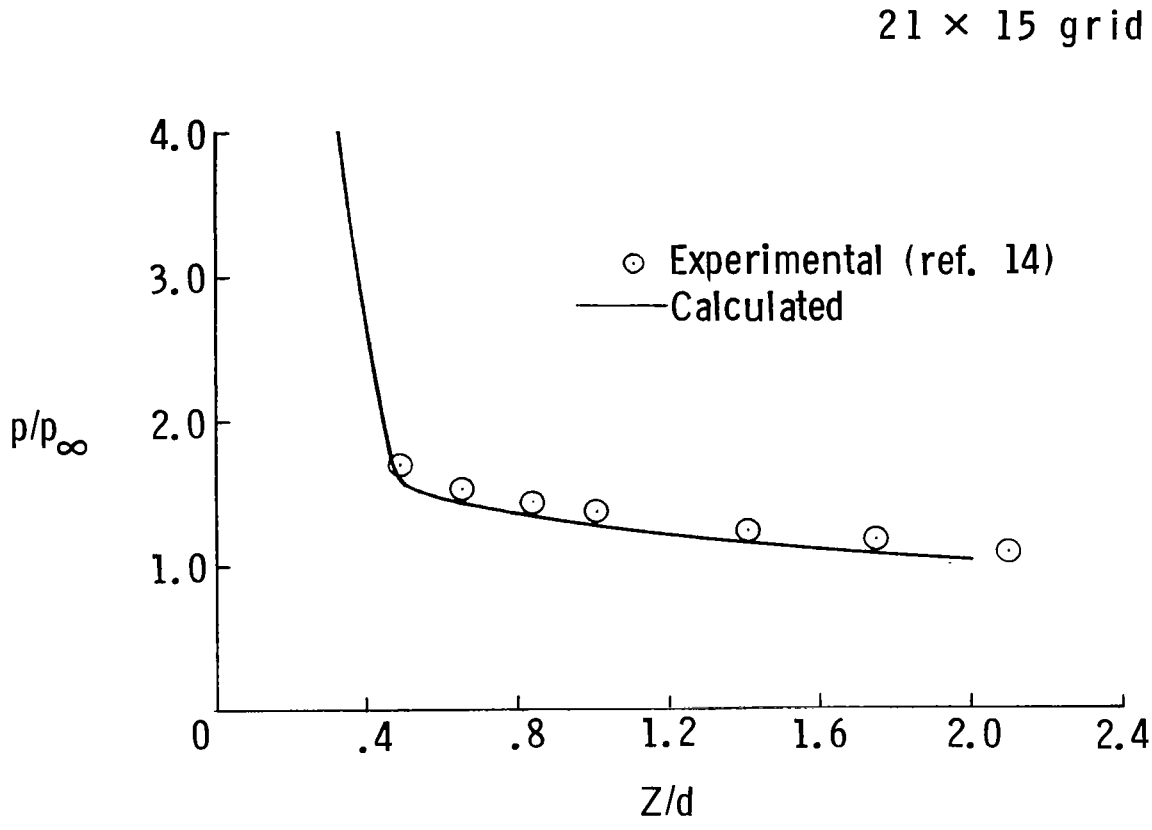

(c) $M_\infty = 5.06$.

Figure 14.- Continued.

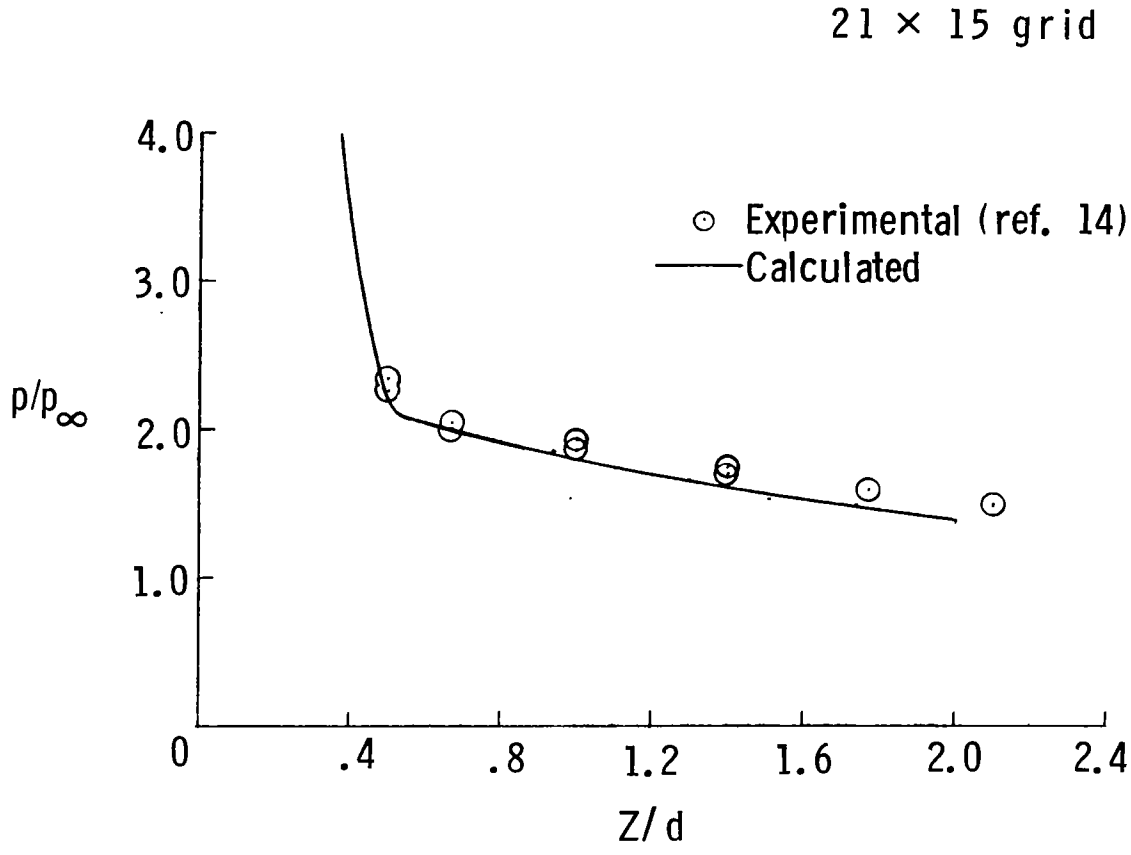

(d) $M_\infty = 6.03$.

Figure 14.- Concluded.

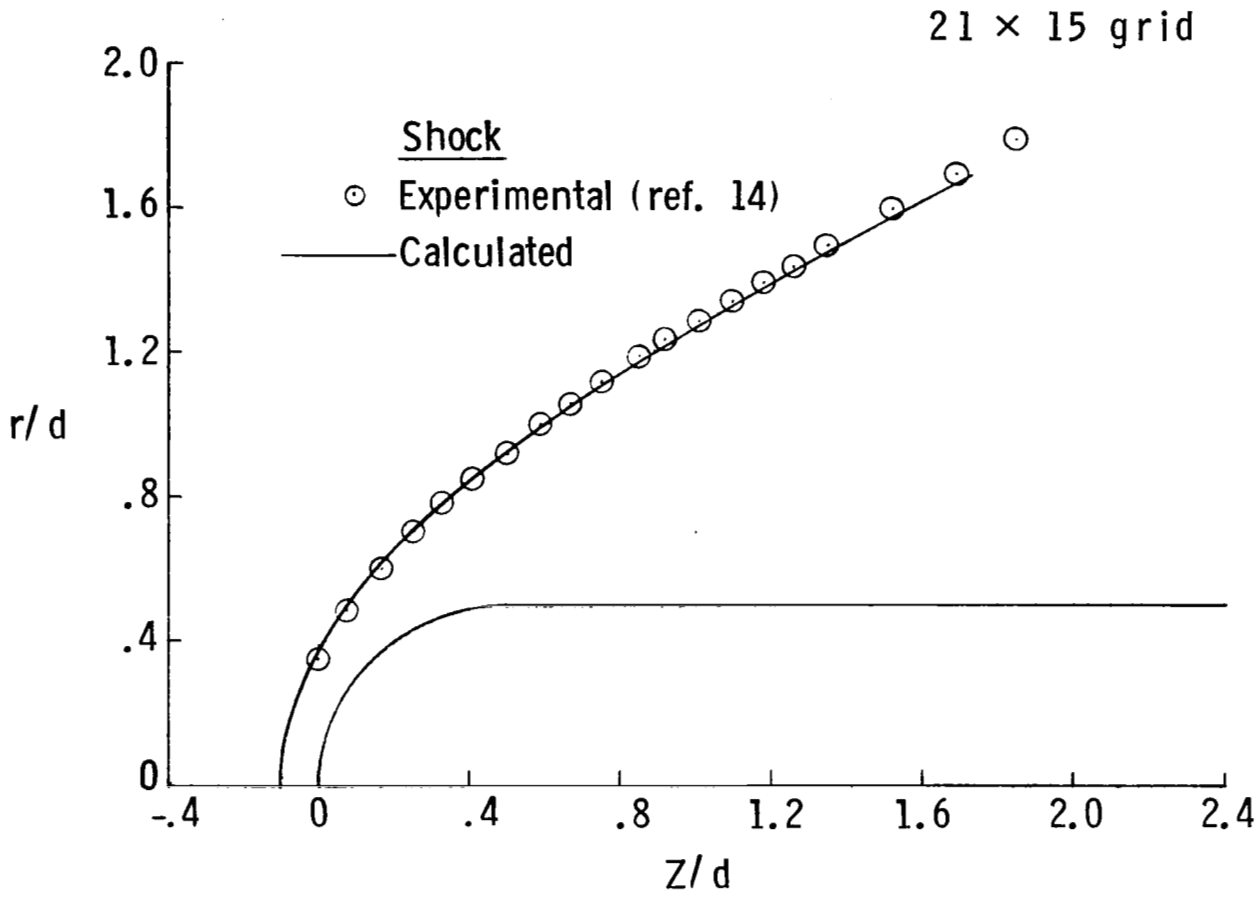

(a) $M_\infty = 3.$

Figure 15.- Shock shape on hemisphere-cylinder. $\gamma = 1.4$.

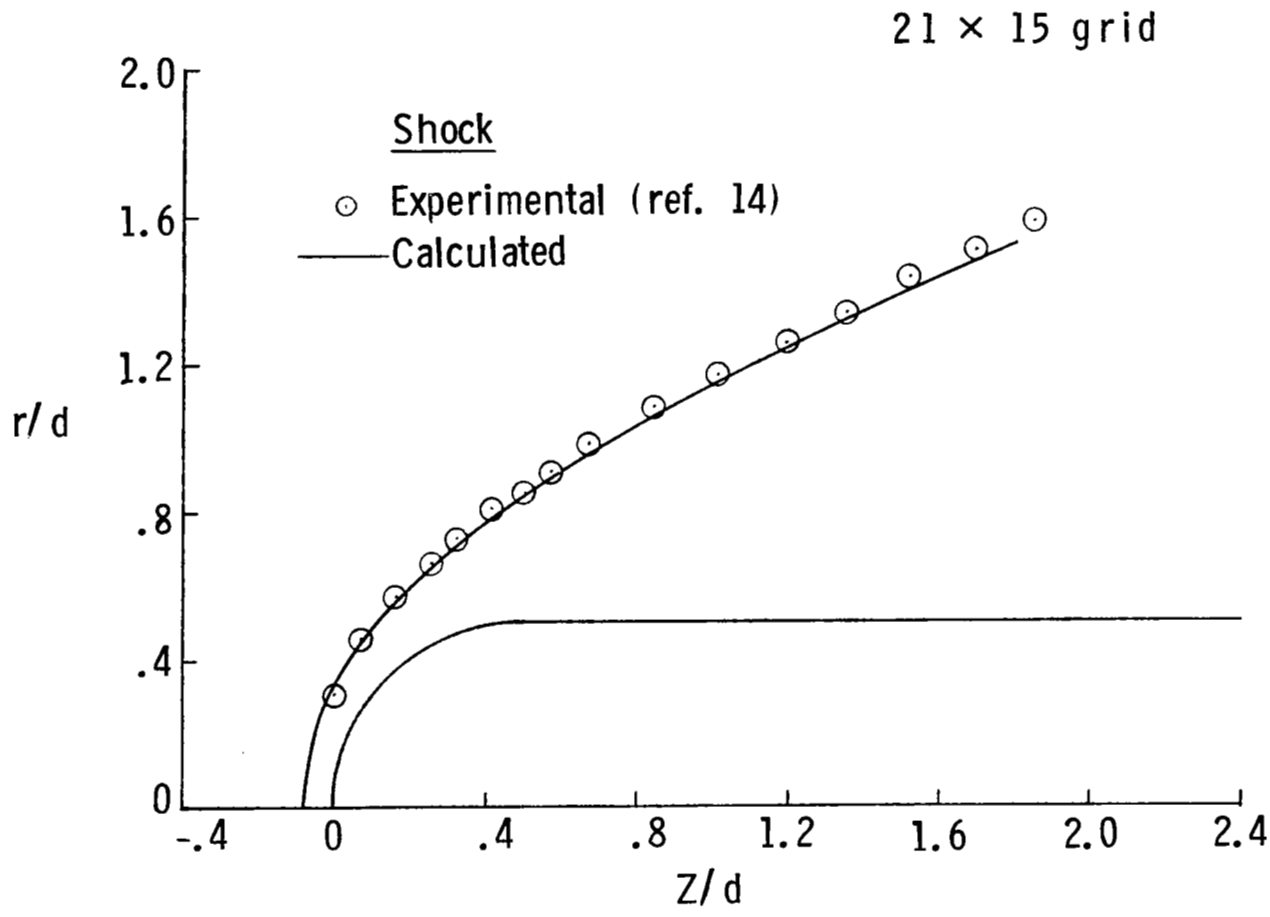

(b) $M_\infty = 4.03$.

Figure 15.- Continued.

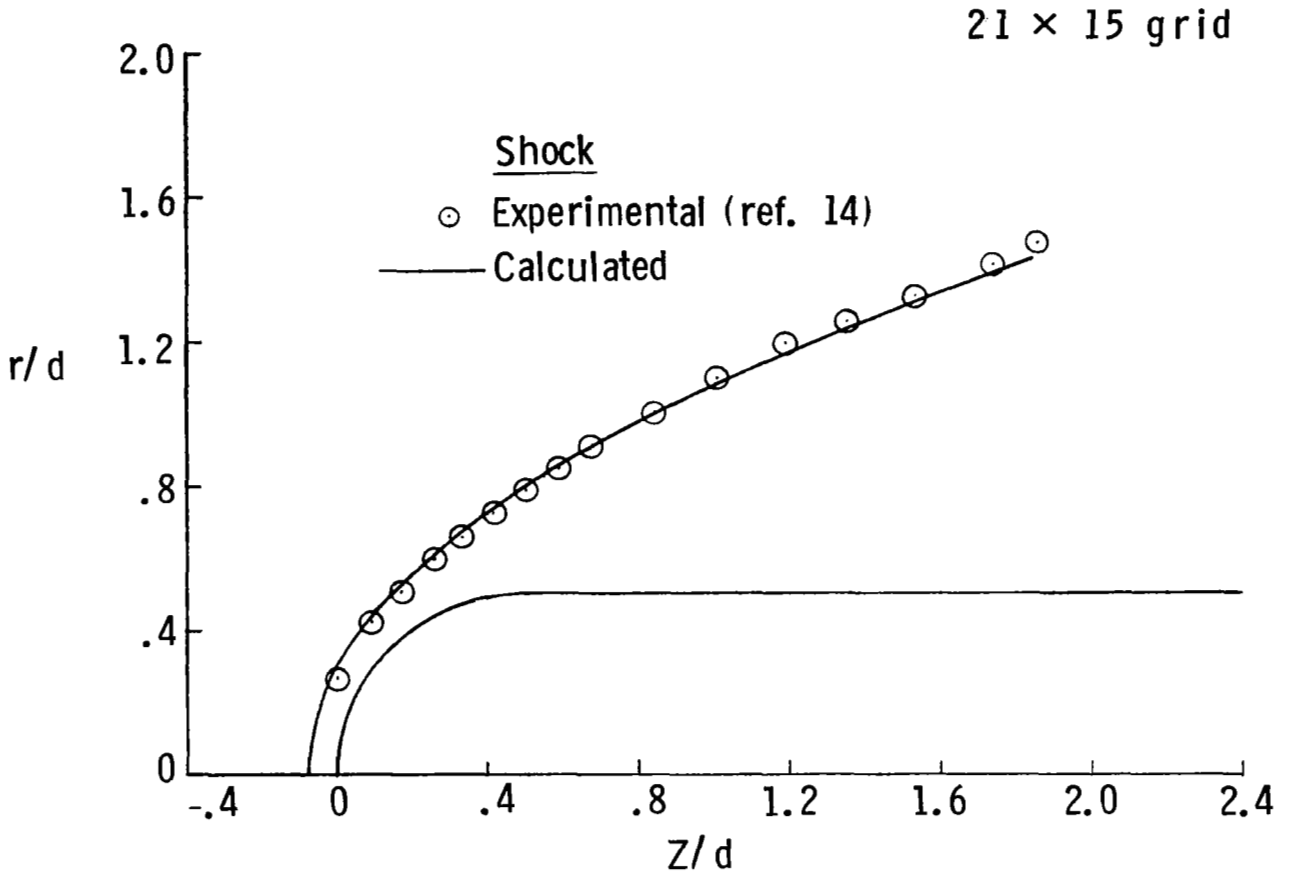

(c) $M_\infty = 5.06$.

Figure 15.- Continued.

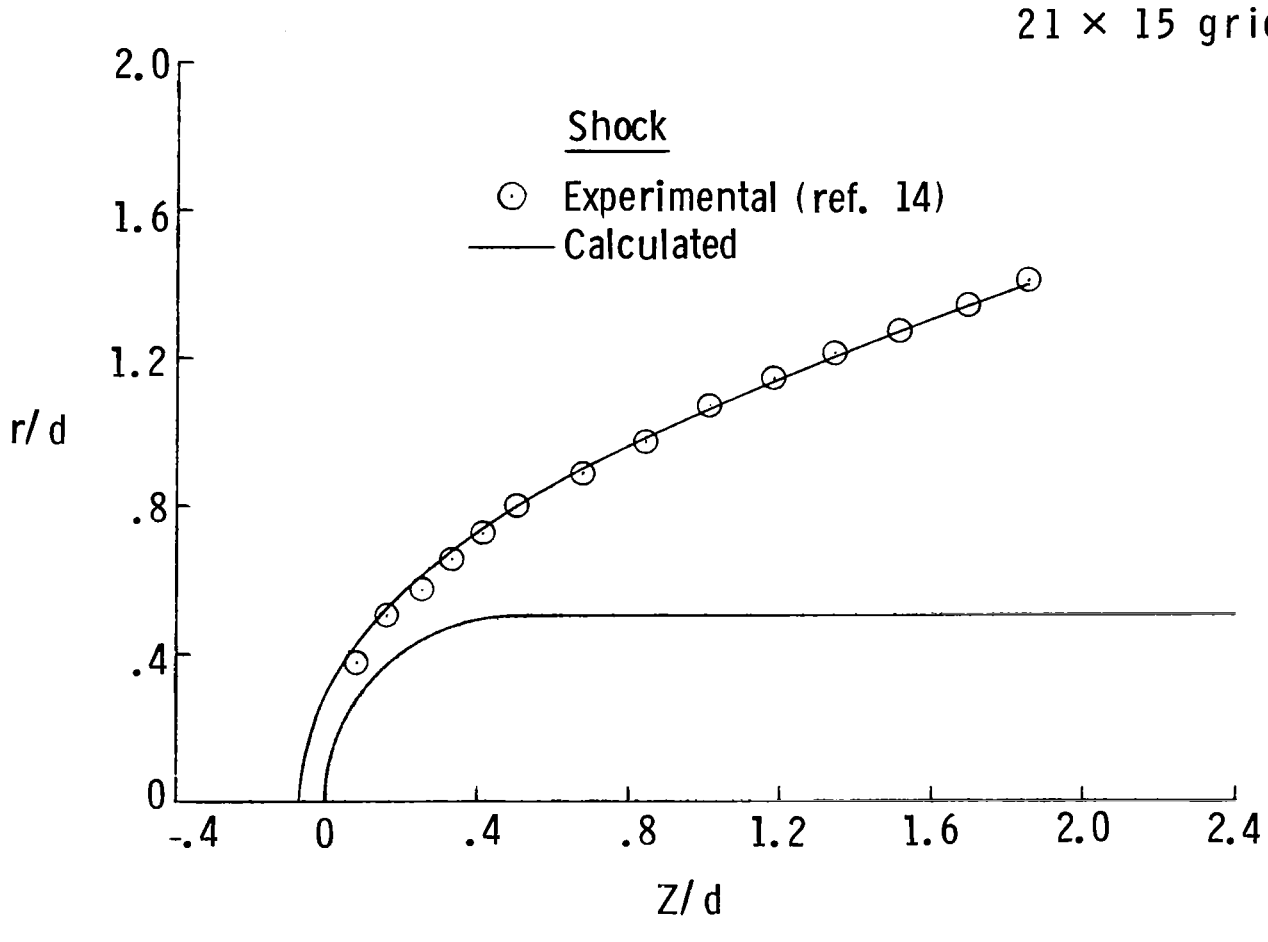

(d) $M_\infty = 6.03$.

Figure 15.- Concluded.

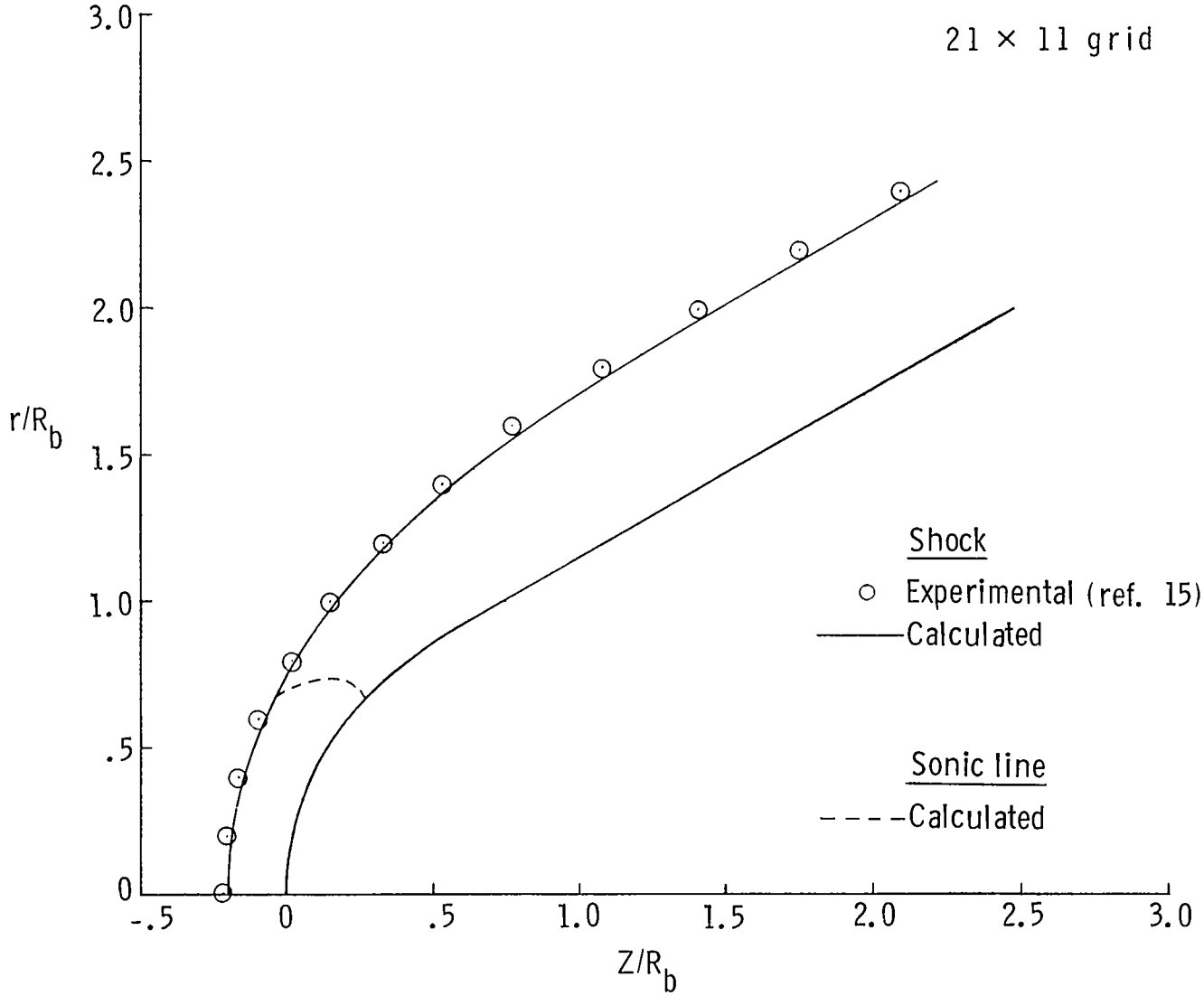

Figure 16.- Shock-wave shape for spherically blunted cone with 30° half-angle in helium. $M_\infty = 20.3$; $\gamma = 1.667$.

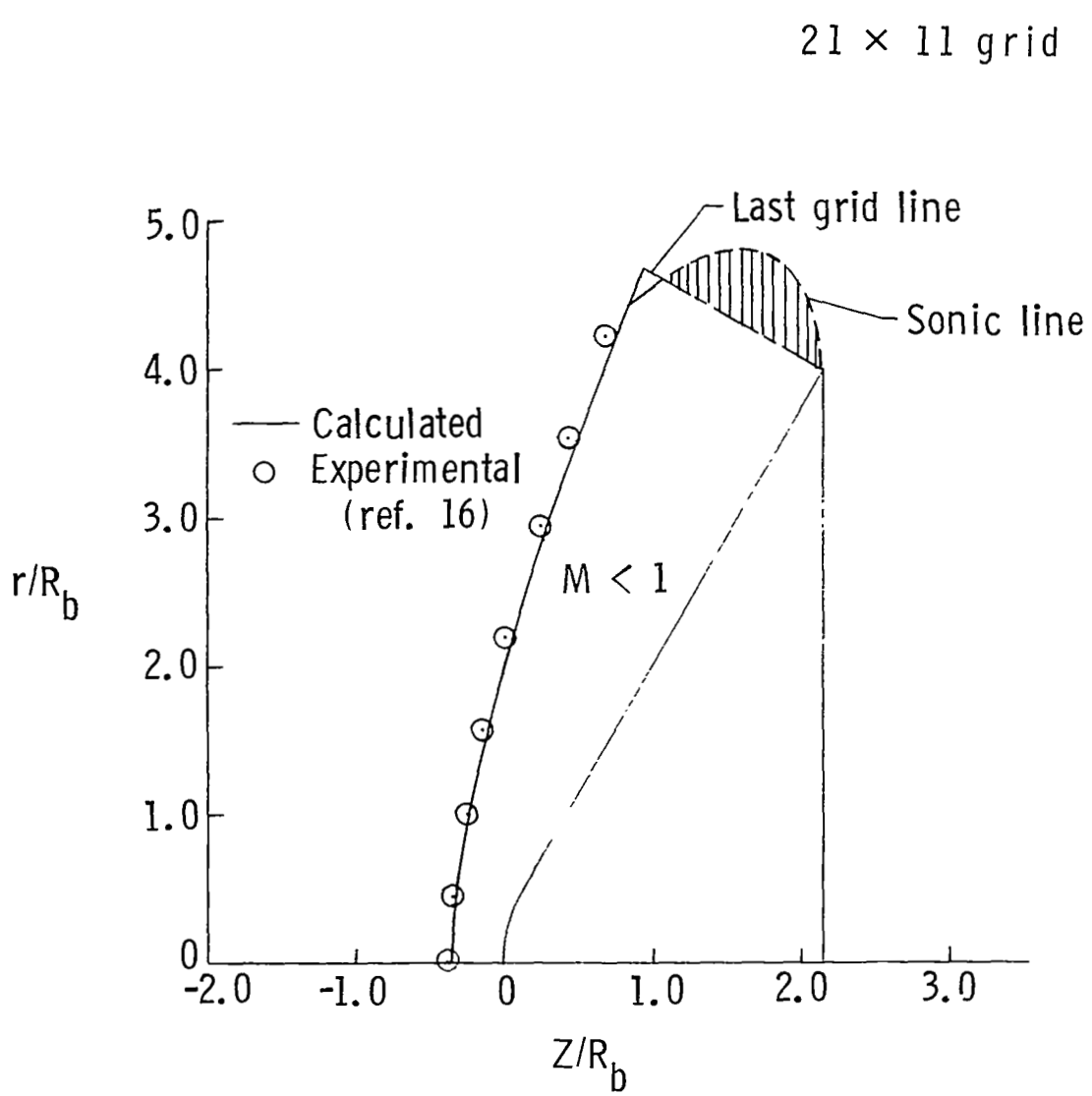

Figure 17.- Shock-wave shape on a spherically blunted cone with 60° half-angle. $M_{\infty} = 4.63$; $\gamma = 1.4$.

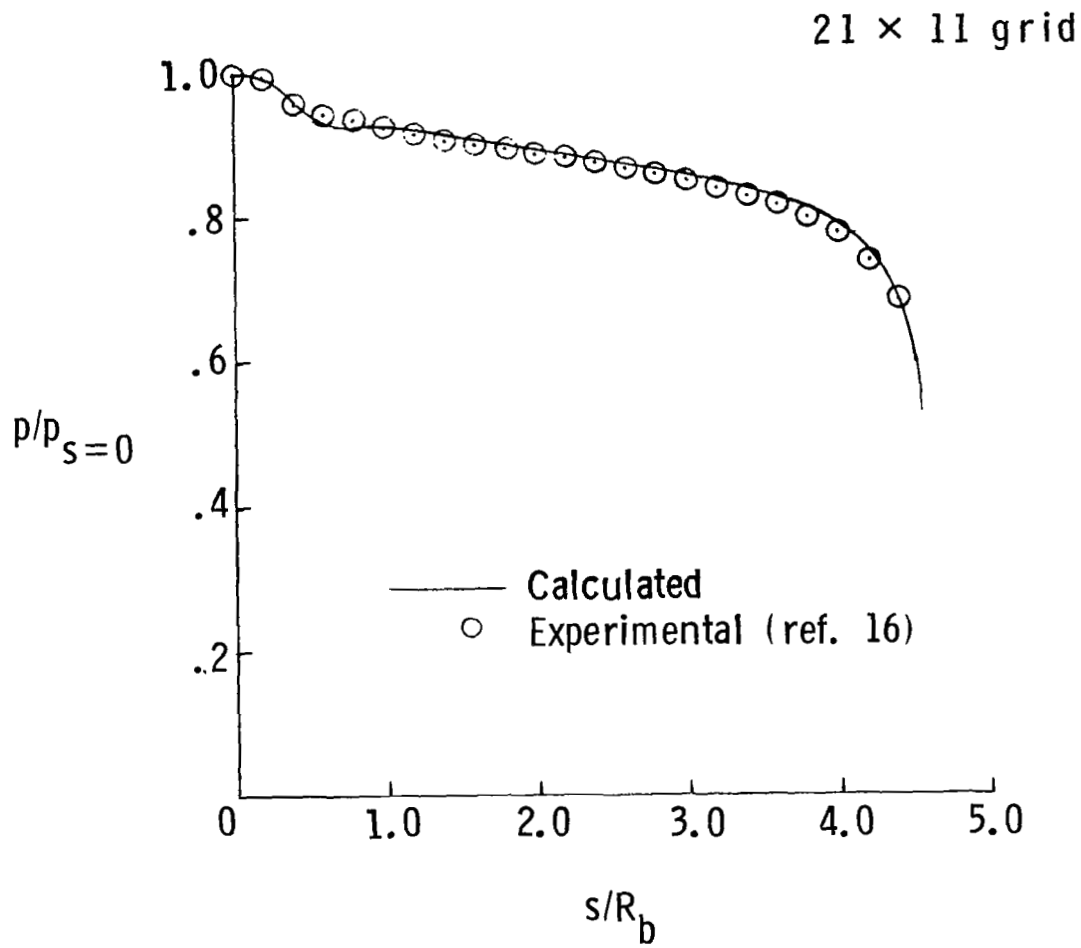

Figure 18.- Pressure distribution on spherically blunted cone with 60° half-angle. $M_{\infty} = 4.63$; $\gamma = 1.4$.

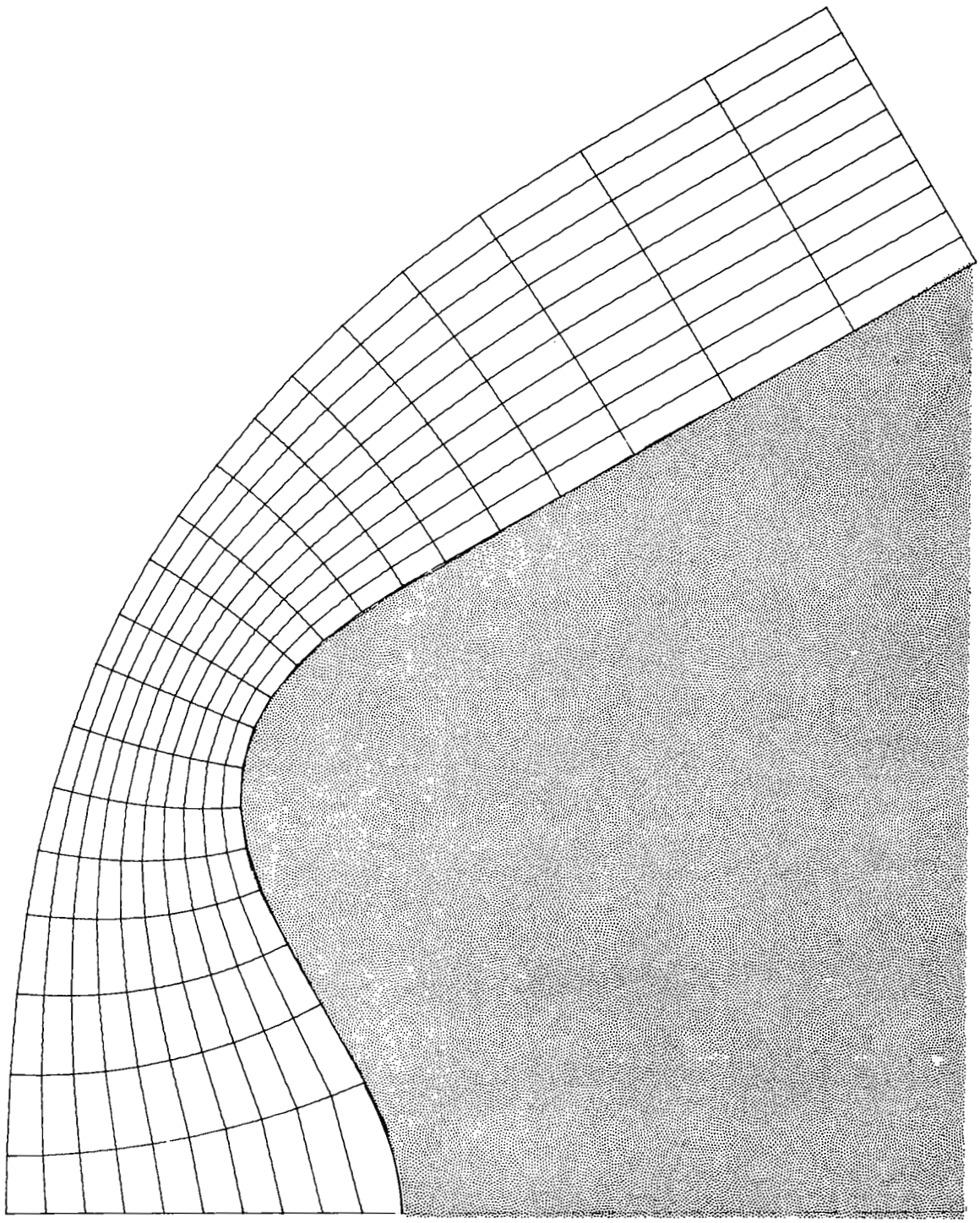

Figure 19.- Coordinate system on reverse curvature body.

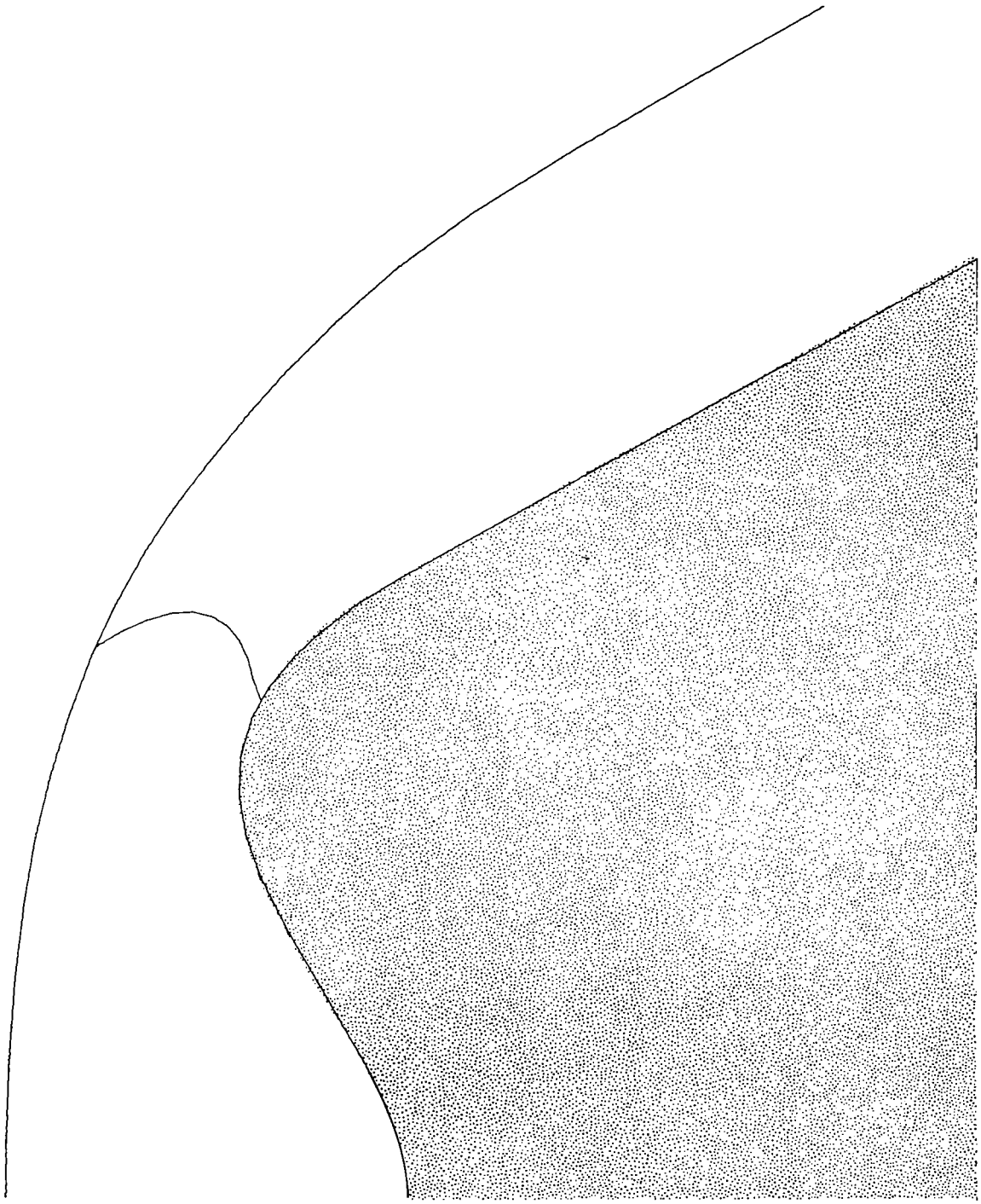

Figure 20.- Shock-wave shape and sonic-line location on reverse curvature body. $M_\infty = 10$; $\gamma = 1.4$.

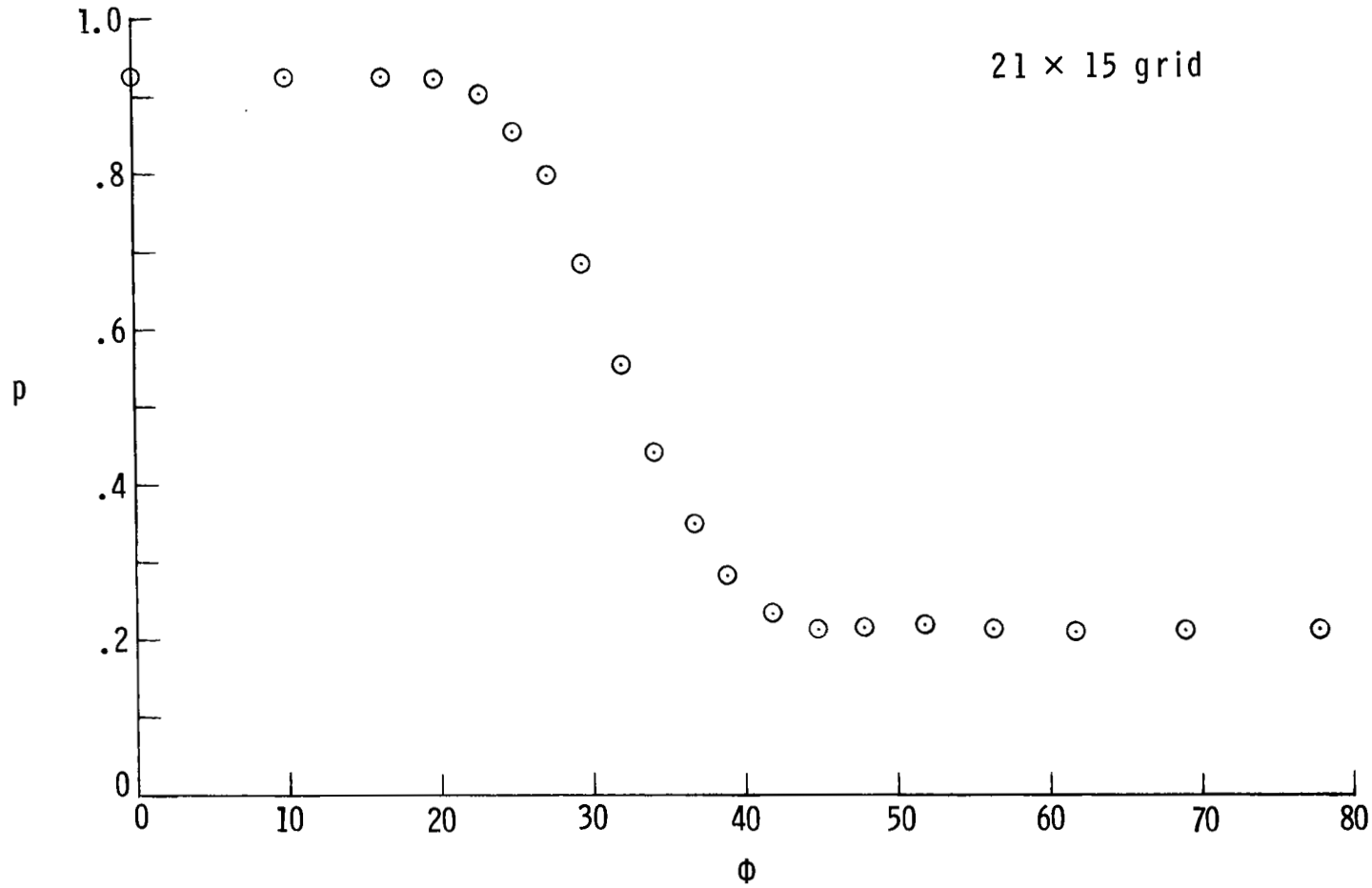

Figure 21.- Pressure distribution on reverse curvature body.
$M_\infty = 10$; $\gamma = 1.4$; $Z_p = 1.0$.

1. Report No.	2. Government Accession No.	3. Recipient's Catalog No.
NASA TP-1619		

4. Title and Subtitle	5. Report Date
APPLICATION OF A NUMERICALLY GENERATED ORTHOGONAL COORDINATE SYSTEM TO THE SOLUTION OF INVISCID AXISYMMETRIC SUPERSONIC FLOW OVER BLUNT BODIES	March 1980
	6. Performing Organization Code
7. Author(s)	8. Performing Organization Report No.
H. Harris Hamilton II, and Randolph A. Graves, Jr.	L-13353
	10. Work Unit No.
9. Performing Organization Name and Address	506-51-13-01
NASA Langley Research Center Hampton, VA 23665	11. Contract or Grant No.
	13. Type of Report and Period Covered
12. Sponsoring Agency Name and Address	Technical Paper
National Aeronautics and Space Administration Washington, DC 20546	14. Sponsoring Agency Code

15. Supplementary Notes

16. Abstract

A numerically generated orthogonal coordinate system (with the body surface and shock wave as opposite boundaries) has been applied with a time asymptotic method to obtain steady-flow solutions for axisymmetric inviscid flow over several blunt bodies including spheres, paraboloids, ellipsoids, hyperboloids, hemisphere cylinders, spherically blunted cones, and a body with a concavity in the stagnation region. Comparisons with experimental data and the results of other computational methods have demonstrated that accurate solutions can be obtained using this approach. The numerically generated orthogonal coordinate system used in the present paper should prove useful for applications to complex body shapes, particularly those with concave regions. In addition, the use of the present orthogonal coordinate system simplifies the form of the governing equations and simplifies the application of boundary conditions at the body surface and shock wave.

17. Key Words (Suggested by Author(s))	18. Distribution Statement
Blunt body Inviscid flow Computational methods	Unclassified - Unlimited Subject Category 02

19. Security Classif. (of this report)	20. Security Classif. (of this page)	21. No. of Pages	22. Price*
Unclassified	Unclassified	58	$5.25

* For sale by the National Technical Information Service, Springfield, Virginia 22161

NASA-Langley, 1980

National Aeronautics and
Space Administration

Washington, D.C.
20546

Official Business
Penalty for Private Use, $300

THIRD-CLASS BULK RATE

Postage and Fees Paid
National Aeronautics and
Space Administration
NASA-451

1 1 1U,A, 031080 S00903DS
DEPT OF THE AIR FORCE
AF WEAPONS LABORATORY
ATTN: TECHNICAL LIBRARY (SUL)
KIRTLAND AFB NM 87117

NASA

POSTMASTER: If Undeliverable (Section 158 Postal Manual) Do Not Return